Modeling the Role of Incisures in Vertebrate Phototransduction

Giovanni Caruso,* Paolo Bisegna,† Lixin Shen,‡ Daniele Andreucci,§ Heidi E. Hamm,‡ and Emmanuele DiBenedetto¶

*Istituto per le Tecnologie della Costruzione, Consiglio Nazionale delle Ricerche, Rome, Italy; †Dipartimento di Ingegneria Civile, Università di Roma Tor Vergata, Rome, Italy; ‡Department of Pharmacology, Vanderbilt University Medical Center, Nashville, Tennessee; §Dipartimento di Metodi e Modelli Matematici, Università di Roma La Sapienza, Rome, Italy; and ¶Department of Mathematics, Vanderbilt University, Nashville, Tennessee

ABSTRACT Phototransduction is mediated by a G-protein-coupled receptor-mediated cascade, activated by light and localized to rod outer segment (ROS) disk membranes, which, in turn, drives a diffusion process of the second messengers cGMP and Ca^{2+} in the ROS cytosol. This process is hindered by disks—which, however, bear physical cracks, known as incisures, believed to favor the longitudinal diffusion of cGMP and Ca^{2+}. This article is aimed at highlighting the biophysical functional role and significance of incisures, and their effect on the local and global response of the photocurrent. Previous work on this topic regarded the ROS as well stirred in the radial variables, lumped the diffusion mechanism on the longitudinal axis of the ROS, and replaced the cytosolic diffusion coefficients by effective ones, accounting for incisures through their total patent area only. The fully spatially resolved model recently published by our group is a natural tool to take into account other significant details of incisures, including their geometry and distribution. Using mathematical theories of homogenization and concentrated capacity, it is shown here that the complex diffusion process undergone by the second messengers cGMP and Ca^{2+} in the ROS bearing incisures can be modeled by a family of two-dimensional diffusion processes on the ROS cross sections, glued together by other two-dimensional diffusion processes, accounting for diffusion in the ROS outer shell and in the bladelike regions comprised by the stack of incisures. Based on this mathematical model, a code has been written, capable of incorporating an arbitrary number of incisures and activation sites, with any given arbitrary distribution within the ROS. The code is aimed at being an operational tool to perform numerical experiments of phototransduction, in rods with incisures of different geometry and structure, under a wide spectrum of operating conditions. The simulation results show that incisures have a dual biophysical function. On the one hand, since incisures line up from disk to disk, they create vertical cytoplasmic channels crossing the disks, thus facilitating diffusion of second messengers; on the other hand, at least in those species bearing multiple incisures, they divide the disks into lobes like the petals of a flower, thus confining the diffusion of activated phosphodiesterase and localizing the photon response. Accordingly, not only the total area of incisures, but their geometrical shape and distribution as well, significantly influence the global photoresponse.

INTRODUCTION

Rod outer segments (ROS), which house the phototransduction apparatus, are made up of highly specialized floating disks. Rod disks house the integral membrane and peripheral membrane proteins that perform photon capture and chemical amplification of the visual signal. Rod disks have clefts called incisures that give the disks a scalloped or lobed appearance when viewed transversely, as in Fig. 1 (1–6). Hundreds of adjacent disks are oriented such that their incisures are longitudinally aligned, and carry vertically parallel microtubules. Disks and incisures are held together with filamentous structures (7) made up of bivalent proteins. Certain of these linking proteins have been identified as members of the tetraspanin family of proteins that form tetramers, retinal degeneration slow (rds)/peripherin, and rom1 (8,9); these are thought to facilitate the curvature of the disk membranes. The stable structure of the disks is mediated by these linking proteins, which take part in their morphogenesis as well as their stability; mutations of these proteins underlie a number of photoreceptor degenerative diseases. Thus incisures are a key conserved structural feature of ROS. Perturbations of such a complex cellular architecture lead to retinal degeneration by triggering apoptosis (10). The structure of the incisures, their geometry and number, varies somewhat with species. Frog and amphibian rods have multiple incisures, whereas rat, mouse, and cow exhibit only a single incisure (11). Even within the same species, red versus green rods have a different number of incisures (12). The depth of the incisures also varies; in frogs they are deep, whereas in human rods they are shallow (12).

The functional role of incisures in phototransduction and the reason for such variations are not known. Because these highly complex structures are found in most vertebrate photoreceptors, and the proteins that make them up are conserved (13,14), the question of their function is clearly significant. This leads to the natural question of their function. Although there have been extensive morphological studies of incisures, as well as biochemical studies of the proteins localized there, no studies on their function have yet been carried out.

Submitted February 17, 2006, and accepted for publication May 8, 2006.

G. Caruso and P. Bisegna contributed equally to this work.

Address reprint requests to E. DiBenedetto, E-mail: em.diben@vanderbilt.edu.

0006-3495/06/08/1192/21 $2.00

doi: 10.1529/biophysj.106.083618

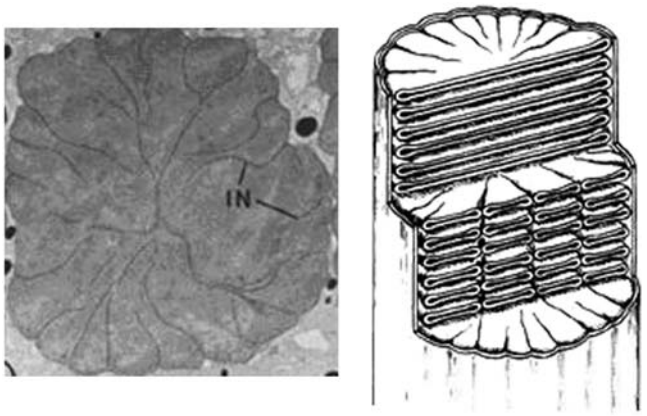

FIGURE 1 (*Left*) Horizontal cross section of frog ROS. (*Right*) Diagram depicting ROS structure. They are reproduced from Papermaster et al. (13).

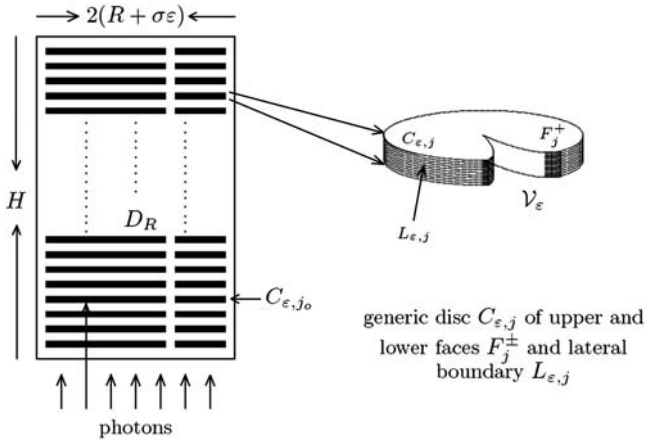

FIGURE 2 Cross section of ROS with a stack of disks with one incisure.

Our study investigates the roles of incisures in visual signal transduction, using a mathematical model of the dynamics of visual transduction that incorporates the geometry of incisures into the model. The computational implementation of the model allows us to vary the number of incisures, as well as their shape and distribution, and determine their effect on the amplitude, spread, and sensitivity of light responses in the absence or presence of variable numbers of incisures.

The presence of incisures should increase the amount of cytoplasm available for diffusion, and thus facilitate diffusion of second messengers. In addition, at least in those species bearing multiple incisures, these divide the disks into lobes like the petals of a flower, thus favoring a localized response to photon activation. For these reasons a model that would account for incisures has to be spatiotemporal in nature, i.e., capable of detecting the diffusion of the second messengers, at each point of the ROS, at all times.

Geometrical setup

The ROS of vertebrates can be assimilated to a right circular cylinder Ω_ε, of height H and radius $R + \sigma\varepsilon$ for some given, positive parameters R, σ, and ε. It houses a stack of n parallel, equal, equispaced, disklike, flattened vesicles (or disks), C_j, $j = 1,2,\ldots,n$, for a given positive integer n, as in Fig. 2. Each of the disks has radius R and thickness ε, they are mutually separated by a distance $\nu\varepsilon$ for a given positive number ν, and they are all coaxial with the cylinder Ω_ε. Although they are not disks, we refer to them as disks, using the common biological terminology. The outer shell of the ROS is a thin cylindrical shell, of thickness $\sigma\varepsilon$ enclosing the ROS as in the left Fig. 3 and whose transversal cross section is depicted in the left Fig. 4. The number n of disks C_j, the parameters H and R, denoting the height of the ROS, and the radius of the disks, as well as the parameters ε, ν, and σ, that quantify the thickness of the disks, their mutual distance, and the thickness of the outer shell, depend on the species. For example, for the Salamander, $n \approx 800$, $H \approx 22\ \mu$m, $R \approx 5.5\ \mu$m, $\varepsilon \approx 14$ nm, and $\nu \approx \sigma \approx 1$ (15).

The disks bear incisures, vertically aligned in series (11, 14,16), whose shape and form are schematically depicted in Fig. 2. The typical incisure starts from the edge of the disk with width of the order of ε, and runs approximately radially toward the center of the disks in a spikelike manner (11,14, 17). According to species they could be as long as the radius of the disk (amphibians, (12)) or less than one-half the radius (rat and monkeys, (12)). They could be in large number ($\approx$17–25 in amphibians and up to 30 in some primates (11)) or there could be only one (rat, mouse, cow (11)).

Phototransduction is mediated by the diffusion of the second messengers cyclic guanosine monophosphate (cGMP) and Ca^{2+} in the cytosol, i.e., the space that remains from Ω_ε when the disks are removed. The movement of molecules, along the longitudinal axis of the ROS is constrained by the hindrance of the disks, their periodically layered structure, and the relatively small thickness of the interdiscal spaces. Incisures, appearing essentially as physical cracks on the disks, are believed to favor the longitudinal diffusion of cGMP and Ca^{2+}.

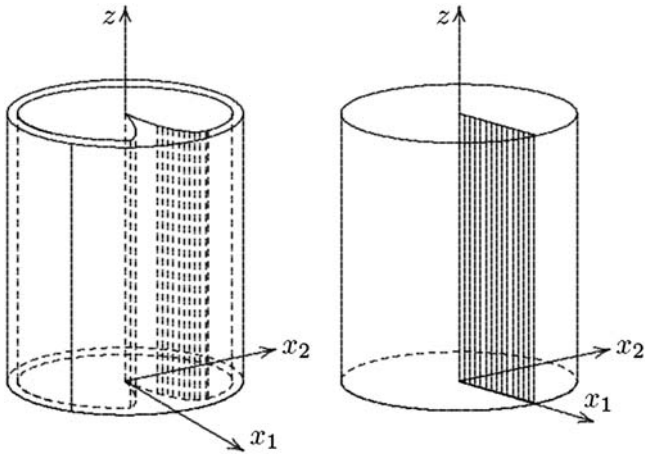

FIGURE 3 (*Left*) Geometrical description of the ROS. (*Right*) The domain obtained in the limit as $\varepsilon \to 0$.

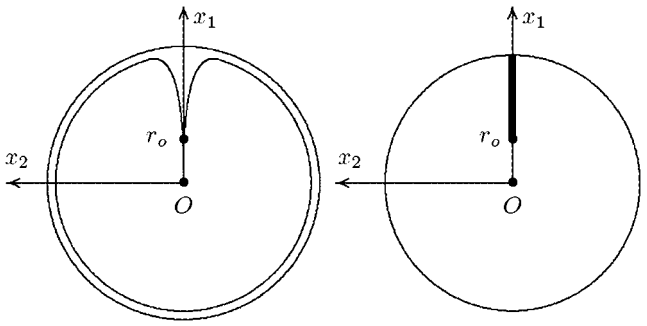

FIGURE 4 (*Left*) Transversal cross section of the ROS. (*Right*) Limit of such a cross section as $\varepsilon \to 0$.

In the Salamander their total area is $\sim 0.8\ \mu m^2$ per disk, or $\sim 1\%$ of the area of the disk (18). Olson and Pugh use this value to give an estimate of the effective longitudinal diffusivity of cGMP in the ROS of amphibians. Holcman and Korenbrot (19) use essentially the same mechanism to account for the incisures in the longitudinal diffusion of the second messengers. In either case, the ROS is regarded as well stirred in the radial variables and the diffusion mechanism is lumped on the longitudinal axis of the rod. The diffusion coefficient is replaced by an effective one, intended to translate somehow, the various physical features, including the presence of the incisures. A similar radially well-stirred approach is also in Gray-Keller et al. (20). From a mathematical point of view, this is equivalent to letting the diffusivity acting on the transversal variables tend to infinity. This raises the question as to what extent a model based on longitudinal diffusion approximates the physical phenomenon.

The main simulation results can be summarized as follows:

1. Effect of the activation site for a given geometrical arrangement of the incisures: moving the activation site toward the rim of the disk (thus inside a lobe of the disk) the global response decreases due to the localization of PDE* induced by disk lobulization. The opposite behavior would be observed if no incisures were present, i.e., the response would increase by moving the activation site toward the rim of the disk.
2. Effect of the disposition of incisures, keeping fixed the total area of incisures and the activation site: the closer the disposition is to the activation site, the higher the response.
3. Effect of incisures on multiple-photon response: incisures increase the response elicited by simultaneous neighboring activation sites, favoring a linear superposition of the corresponding single photon responses (SPR).

LOCAL MODELING AND SURFACE-VOLUME INTERACTIONS

The plasma membrane forming the lateral boundary of the ROS contains cGMP-gated channels. In the dark, a fraction of these channels are open, permitting influx of Na^+ and Ca^{2+} ions. An exchanger located on the same plasma membrane extrudes Ca^{2+} and K^+ while permitting additional Na^+ influx. The exchange rate varies with internal Ca^{2+} concentration. In the dark, Ca^{2+} and cGMP are at a steady state and their steady-state or dark concentrations are denoted by $[Ca^{2+}]_{dark}$ and $[cGMP]_{dark}$. Absorption of a photon by a rhodopsin molecule residing on an outer segment disk initiates a cascade *receptor* $\rightarrow$ *transducer* $\rightarrow$ *effector*, whose net effect is to produce a sink (a negative source term) for cGMP produced by the activated effector phosphodiesterase (PDE*). The cGMP is then depleted by diffusion toward such a sink. Depletion of cGMP causes closing of the channels thereby reducing the inward current. We refer to Pugh and Lamb (15) for a detailed description of such a process.

The geometry of the ROS enters in this process on several accounts. First, the current is generated on the outer membrane since this is where the cGMP-gated channels reside. Second, the incisures reduce the hindrance of the disks on the longitudinal movement of cGMP. We refer to Andreucci et al. (21) for a discussion on the effects of diffusion, its localized nature, and on the notion of pointwise versus bulk modeling. The space available for diffusion of cGMP and Ca^{2+} is

$$\tilde{\Omega}_\varepsilon = \Omega_\varepsilon - \bigcup_{j=1}^{n} \bar{C}_j. \tag{1}$$

Denote by Ω the cylinder of height H and radius R, formally obtained from Ω_ε by setting $\varepsilon = 0$. Denote also by $\mathcal{V}_\varepsilon$ the two-dimensional, transversal cross section of one such incisure as in Fig. 2, and let $\mathcal{B}_\varepsilon = \mathcal{V}_\varepsilon \times (0,H)$ the bladelike cylindrical domain cut by incisures in the ROS, as in the left Fig. 3.

The stack of incised disks, C_j, identifies and is included in the right cylinder, Ω–$\mathcal{B}_\varepsilon$. The indicated geometry implies that the ratio of the volume of the stack of disks C_j to the volume of Ω–$\mathcal{B}_\varepsilon$ is independent of the parameter ε, i.e.,

$$\frac{vol(\cup_{j=1}^{n} C_j)}{vol(\Omega - \mathcal{B}_\varepsilon)} = \frac{1}{1+\nu} \stackrel{\text{def}}{=} \gamma_o. \tag{2}$$

According to the system of coordinates introduced in Fig. 3, $\bar{x} = (x_1, x_2)$ denote the transversal variables and z is the longitudinal variable along the axis of the ROS. In this system, the outer shell is described by

$$\Sigma_\varepsilon = \{(\bar{x}, z) | R < |\bar{x}| < R + \sigma\varepsilon; z \in (0,H)\}. \tag{3}$$

Locality of photocurrent

The current density due to Ca^{2+} exchange, across the ROS lateral surface, is given by a Michaelis-Menten-type relation

$$J_{ex} = \frac{j_{ex}^{sat}}{\Sigma_{rod}} \frac{[Ca^{2+}]}{K_{ex} + [Ca^{2+}]}, \tag{4}$$

where j_{ex}^{sat} is the saturated exchange current (as $[Ca^{2+}] \to \infty$), K_{ex} is the Ca^{2+} concentration at which the exchange rate

is half-maximal, and $\Sigma_{\rm rod}$ is the surface area of the lateral boundary S_ε of the ROS.

At fixed membrane voltage, the current density $J_{\rm cG}$ carried by the cGMP-gated channels, across the ROS lateral surface, is given by the Hill-type relation

$$J_{\rm cG} = \frac{j_{\rm cG}^{\max}}{\Sigma_{\rm rod}} \frac{[\rm cGMP]^{m_{\rm cG}}}{K_{\rm cG}^{m_{\rm cG}} + [\rm cGMP]^{m_{\rm cG}}}, \tag{5}$$

where $j_{\rm cG}^{\max}$ is the maximal cGMP-current (as $[\rm cGMP] \to \infty$), $m_{\rm cG}$ is the Hill exponent, and $K_{\rm cG}$ is the half-maximum channel-opening concentration of cGMP.

It is pointed out that $J_{\rm ex}$ and $J_{\rm cG}$ are current densities (i.e., current per unit area, measured in pA/μm^2), and, in general, take different values at different points of the lateral boundary S_ε of the ROS. Indeed, Eqs. 4 and 5 are local in nature, i.e., they provide the current densities in terms of space-time values of [cGMP] and [Ca^{2+}]. Since current is generated at the lateral boundary of the ROS, this is where the values of [cGMP] and [Ca^{2+}] are relevant for the computation of $J_{\rm cG}$ and $J_{\rm ex}$. Equations 4 and 5 imply that a local pointwise evaluation of these currents requires a pointwise description of [cGMP] and [Ca^{2+}] as functions of position and time. In the literature, these currents are regarded as volumic, as if they were distributed over the entire ROS. In particular in Nikonov et al. (22), volumic current densities are defined by dividing the coefficients $j_{\rm cG}^{\max}$ and $j_{\rm ex}^{\rm sat}$ by the volume of the cytosol ($\approx$1 pl).

In absence of light, $J_{\rm ex}$ and $J_{\rm cG}$ are constant and equal to their dark values:

$$\begin{aligned} J_{\rm ex;dark} &= J_{\rm ex}\big|_{t=0} = \frac{j_{\rm ex}^{\rm sat}}{\Sigma_{\rm rod}} \frac{[\rm Ca^{2+}]_{\rm dark}}{K_{\rm ex} + [\rm Ca^{2+}]_{\rm dark}} \\ J_{\rm cG;dark} &= J_{\rm cG}\big|_{t=0} = \frac{j_{\rm cG}^{\max}}{\Sigma_{\rm rod}} \frac{[\rm cGMP]_{\rm dark}^{m_{\rm cG}}}{K_{\rm cG}^{m_{\rm cG}} + [\rm cGMP]_{\rm dark}^{m_{\rm cG}}}. \end{aligned} \tag{6}$$

The local value of (total) current density $J_{\rm loc}$ and its dark value $J_{\rm dark}$ are defined as

$$J_{\rm loc}(\theta, z, t) = J_{\rm ex}(\theta, z, t) + J_{\rm cG}(\theta, z, t); \quad J_{\rm dark} = J_{\rm loc}\big|_{t=0}. \tag{7}$$

As z ranges over $(0, H)$ and θ ranges over $[0, 2\pi)$, the variables (θ, z) range over the lateral boundary S_ε of the ROS.

At time $t = 0$, both [Ca^{2+}] and [cGMP] are constant and equal to their dark values. Consequently $J_{\rm dark}$ is also a constant, and the global current across the plasma membrane at time $t = 0$ is

$$j_{\rm dark} = \Sigma_{\rm rod} J_{\rm dark}. \tag{8}$$

The local response to light activation, at time t, at a point (θ, z) of the plasma membrane, is the variation of $J_{\rm loc}(\theta, z, t)$ from its dark value, i.e., $J_{\rm dark}$–$J_{\rm loc}(\theta, z, t)$. Define the global current across the entire plasma membrane as

$$j(t) = \int_{S_\varepsilon} J_{\rm loc}(\theta, z, t) dS, \tag{9}$$

where dS is the surface measure of the lateral boundary S_ε of the ROS. Results are presented in terms of the relative responses

$$1 - \frac{J_{\rm loc}(\theta, z, t)}{J_{\rm dark}}; \quad 1 - \frac{j(t)}{j_{\rm dark}}. \tag{10}$$

Local spread of activation

Denote by (θ, z) the coordinates of the lateral boundary S_ε of the ROS, and let $P_* = (x_{1,*}, x_{2,*}, z_*)$ be the activated point. Thus z_* is the z location of the activated disk, and $(x_{1,*}, x_{2,*})$ is the point on the activated disk where isomerization occurs. At each fixed time t, the local response $J_{\rm dark} - J_{\rm loc}(\theta, z, t)$ is highest at $z = z_*$, it decreases away from z_*, and it becomes negligible sufficiently away from z_*. That interval at z_*, along the longitudinal axis of the ROS, where the current suppression is not negligible, defines (roughly speaking) the interval of spread of the response to light activation. This localization has been pointed out by a number of researchers (18,20,23–26), and it is generally accepted that the response is local in the sense that the interval of spread of the response to light activation is considerably smaller than the length of the outer segment. However, the literature does not contain an unambiguous quantitative notion of spread. A discussion on this issue is provided in Caruso et al. (27).

Choose $\delta \in (0, 1)$ and define spread of excitation as the width $\lambda(\theta, \delta, t)$ of the largest interval at z_*, along the longitudinal axis of the rod, at a fixed angle θ and time t, where the response is greater than a fixed fraction δ of the dark circulating current, at that time. Precisely, assuming that $\zeta \to J_{\rm loc}(\theta, z_* \pm \zeta, t)$ for fixed θ, z_*, and t is increasing for $\zeta > 0$, the spread is given by

$$\lambda(\theta, \delta, t) = \zeta_1 + \zeta_2,$$

where ζ_1 and ζ_2 are two positive numbers such that

$$\begin{aligned} J_{\rm dark} - J_{\rm loc}(\theta, z_* + \zeta_1, t) &= \delta J_{\rm dark}, \\ J_{\rm dark} - J_{\rm loc}(\theta, z_* - \zeta_2, t) &= \delta J_{\rm dark}. \end{aligned} \tag{11}$$

Here, δ is a positive parameter that most likely encompasses some biological features of the process. We are in the process of investigating the mathematical link of δ with the underlying biology. However, whatever the biological interpretation, Eq. 11 is a precise and mathematically unambiguous notion of spread. For computational purposes, we have chosen $\delta = 0.5\%$. Further discussion on the notion of spread of activation is provided in How Incisures Affect the Spread of the Response.

THE FULL THREE-DIMENSIONAL MODEL

The concentrations [cGMP] and [Ca^{2+}] are smooth functions of space and time, defined in the domain $\tilde{\Omega}_\varepsilon$, available for diffusion, and they satisfy the mass balance equations within

such a domain. Since in the cytosol there are no volume sources,

$$\frac{\partial[\mathrm{cGMP}]}{\partial t} - \mathrm{div}(D_{\mathrm{cG}}\nabla[\mathrm{cGMP}]) = 0$$
$$\frac{\partial[\mathrm{Ca}^{2+}]}{\partial t} - \mathrm{div}(D_{\mathrm{Ca}}\nabla[\mathrm{Ca}^{2+}]) = 0 \,\mathrm{in}\,\tilde{\Omega}_\varepsilon, \qquad (12)$$

where t is time and ∇ is the gradient in the spatial variables $(\bar{x}, z)$. The coefficients D_{cG} and D_{Ca} are the respective diffusion coefficients of cGMP and Ca^{2+} in the cytosol. For a dark-adapted rod, the initial data for the concentrations [cGMP] and $[Ca^{2+}]$ are their uniform, steady-state, dark values

$$[\mathrm{cGMP}]|_{\mathrm{t}=0} = [\mathrm{cGMP}]_{\mathrm{dark}} \quad \text{and} \quad [\mathrm{Ca}^{2+}]|_{\mathrm{t}=0} = [\mathrm{Ca}^{2+}]_{\mathrm{dark}}. \qquad (13)$$

Boundary fluxes of [cGMP]

Production or depletion of cGMP occurs through binding phenomena on the faces $F_{\mathrm{j}}^{\pm}$ of the disks C_{j}. Accordingly these terms are modeled as fluxes across such faces.

Basal PDE hydrolyzes cGMP at all disk faces. The rate of cGMP depletion (per unit surface area, per unit time, i.e., depletion flux of cGMP), due to basal PDE, is given by

$$k_{\sigma;\mathrm{hyd}}[\mathrm{PDE}]_\sigma[\mathrm{cGMP}] \quad \text{on the faces } F_{\mathrm{j}}^{\pm}.$$

Here, $[\mathrm{PDE}]_\sigma$ denotes the surface density of PDE (in number of molecules per μm^2) and $k_{\sigma;\mathrm{hyd}}$ is the surface hydrolysis rate (in $[\mathrm{No.}/\mu m^3]^{-1}\ s^{-1}$). Accordingly, $k_{\sigma;\mathrm{hyd}}[\mathrm{PDE}]_\sigma$ has dimensions of $\mu m\ s^{-1}$. These terms, the significance of their surface formulation, as opposed to their volumetric counterparts (20,22,28), have been discussed and estimated in Caruso et al. (27). The previous equation was shown to lead to

$$k_{\sigma;\mathrm{hyd}}[\mathrm{PDE}]_\sigma[\mathrm{cGMP}] = \frac{1}{2}\nu\varepsilon\beta_{\mathrm{dark}}[\mathrm{cGMP}] \quad \text{on the faces } F_{\mathrm{j}}^{\pm}. \qquad (14)$$

For the Salamander, we estimated $\beta_{\mathrm{dark}} \approx 1\ s^{-1}$.

Production of cGMP is mediated by guanylyl cyclase (GC), which is located on the faces of the disks C_{j}. Molecules of guanosine triphosphate (GTP) bind to molecules of GC to synthesize cGMP. Such activity is modulated by Ca^{2+}, being maximum for $[Ca^{2+}] = 0$ and minimum for $[Ca^{2+}] \to \infty$. In Andreucci et al. (21) and Caruso et al. (27), the surface/volume nature of such a production rate was analyzed and it was shown that the cGMP production rate may be described by the relation

$$k_{\{\mathrm{GC;o}\}}[\mathrm{GC}]_\sigma = \frac{1}{2}\nu\varepsilon\alpha \quad \text{on the faces } F_{\mathrm{j}}^{\pm}, \qquad (15)$$

where

$$\alpha = \alpha_{\min} + \frac{\alpha_{\max} - \alpha_{\min}}{1 + ([\mathrm{Ca}^{2+}]/K_{\mathrm{cyc}})^{m_{\mathrm{cyc}}}}. \qquad (16)$$

Here, $\alpha_{\min} < \alpha_{\max}$ are given positive constants and K_{cyc} is a scaling Ca^{2+} concentration for the cyclase effect, and m_{cyc} is the Hill exponent. Also, $[\mathrm{GC}]_\sigma$ is the surface density of GC and $k_{\{\mathrm{GC;o}\}}$ is the corresponding surface catalytic rate. For the Salamander, these parameters have been estimated in Caruso et al. (27), by combining their volumetric analogs appearing in the literature, with the indicated surface/volume interpretation.

Let $C_{\mathrm{j}*}$ be a disk hit by one or several photons on one of its faces, say, for example, $F_{\mathrm{j}_*}^{-}$, and let $[\mathrm{PDE}^*]_\sigma(\bar{x}, t)$ be the resulting surface density of activated PDE (in number of PDE subunits per μm^2), as a function of space and time. Let also $k^*_{\sigma;\mathrm{hyd}}$ denote the surface catalytic rate of light-activated PDE (measured in $[(\mathrm{number\ of\ molecules})/\mu m^3]^{-1}\ s^{-1}$). The flux generated on $F_{\mathrm{j}_*}^{-}$ by such a depletion of cGMP is then

$$k^*_{\sigma;\mathrm{hyd}}[\mathrm{PDE}^*]_\sigma[\mathrm{cGMP}]. \qquad (17)$$

The surface/volume nature of such a formula has been discussed in Andreucci et al. (21) and Caruso et al. (27) and the parameter $k^*_{\sigma;\mathrm{hyd}}$ for the Salamander has been estimated as $k^*_{\sigma;\mathrm{hyd}} \approx 1\ \mu m^3\ s^{-1}\ \mathrm{No.}^{-1}$. The determination of the function $[\mathrm{PDE}^*]_\sigma(\bar{x}, t)$ will be discussed in the context of The Activation Mechanism. The above considerations yield the following boundary condition for [cGMP] on each of the faces $F_{\mathrm{j}}^{\pm}$, $j = 1,\ldots,n$,

$$-D_{\mathrm{cG}}\frac{\partial}{\partial z}[\mathrm{cGMP}]|_{F_{\mathrm{j}}^{\pm}} = \frac{1}{2}\nu\varepsilon(\pm\alpha \mp \beta_{\mathrm{dark}}[\mathrm{cGMP}]) + \delta_{\mathrm{j}}k^*_{\sigma;\mathrm{hyd}}[\mathrm{PDE}^*]_\sigma[\mathrm{cGMP}], \qquad (18)$$

where δ_{j} equals 1 if $j = j_*$ (activated face) and it is zero otherwise. We finally assume that cGMP does not penetrate the lateral part L_{j} of the disks C_{j}, nor does it outflow the ROS, i.e.,

$$D_{\mathrm{cG}}\nabla[\mathrm{cGMP}]\cdot\mathbf{n}|_{L_{\mathrm{j}}} = 0; \quad D_{\mathrm{cG}}\nabla[\mathrm{cGMP}]\cdot\mathbf{n}|_{\partial\Omega_\varepsilon} = 0, \qquad (19)$$

where $\mathbf{n}$ is the unit normal to the indicated surfaces pointing outside the ROS.

If n_* disks are activated, each by one or several photons, at either their lower or upper faces $F_{\mathrm{j}_*}^{\pm}$, we relabel and order them as $C_{\mathrm{j}*}$ for $j_* = 1,\ldots,n_*$. Then the flux conditions on the faces $F_{\mathrm{j}}^{\pm}$ are expressed as in Eq. 18, where δ_{j} equals 1 if $j \in \{1,\ldots,n_*\}$ and it is zero otherwise.

Boundary conditions for $[Ca^{2+}]$

$[Ca^{2+}]$ flows into the cytosol through cGMP-gated channels and is extruded by the electrogenic exchanger. Thus the boundary fluxes for $[Ca^{2+}]$ can be expressed as

$$-D_{\mathrm{Ca}}\nabla[\mathrm{Ca}^{2+}]\cdot\mathbf{n} = \frac{1}{B_{\mathrm{Ca}}\mathcal{F}}\left(J_{\mathrm{ex}} - \frac{1}{2}f_{\mathrm{Ca}}J_{\mathrm{cG}}\right). \qquad (20)$$

The current densities J_{ex} and J_{cG} (measured in $\mathrm{pA}/\mu m^2$) were defined in Eqs. 4 and 5. The constant B_{Ca} is the buffering power of the cytoplasm for Ca^{2+}, f_{Ca} is the fraction of

cGMP-activated current carried by Ca^{2+}, and $\mathcal{F}$ is the Faraday constant.

In Nikonov et al. (22), the currents J_{ex} and J_{cG} contribute with a volumic term to the variation of $[Ca^{2+}]$, i.e., j_{ex}^{sat} and j_{cG}^{max} are divided by the volume V_{cyt}, of the cytosol in the ROS ($\approx$1 pl). Since both currents are generated on the lateral boundary of the ROS and are local in nature, they are taken here as surface current densities and thus as boundary sources for $[Ca^{2+}]$.

Calcium does not penetrate the disk C_j, nor does it outflow the ROS through its top $\{z = H\}$ or its bottom $\{z = 0\}$. Therefore,

$$\nabla[Ca^{2+}]|_{\partial C_j} \cdot \mathbf{n}_j = 0 \text{ and } \frac{\partial[Ca^{2+}]}{\partial z} = 0 \quad \text{for } z = 0 \text{ and } z = H, \tag{21}$$

where $\mathbf{n}_j$ is the unit normal to C_j.

The full pointwise, three-dimensional space-time model for [cGMP] and $[Ca^{2+}]$ consists of the partial differential Eq. 12, the initial conditions Eq. 13, and the boundary conditions Eqs. 18–21.

THE HOMOGENIZED MODEL

Using an idea first introduced in Andreucci et al. (21,29), the homogenized model is derived by regarding ε as a small parameter to be let go to zero, starting from its initial physical value $\varepsilon_o = 14$ nm. The limit process keeps constant the volume fraction of the ROS available for diffusion. As $\varepsilon \to 0$ the disks C_j, the incisures $\mathcal{V}_\varepsilon$, and the bladelike regions $\mathcal{B}_\varepsilon$ become thinner and thinner. In the limiting process, we artificially increase the number of disks C_j in such a way that the volume fraction γ_o in Eq. 2 remains constant. The interdiscal spaces are also thin, of the order of ε; however, there are, roughly speaking, ε^{-1} of them, so the information in them is compounded in the limit. The faces $F_{j_*}^-$ where a photon is captured are at levels z_{j*} for $j_* = 1,2,\ldots,n_*$. The limit is carried out so that the levels z_{j*} are kept fixed for all $\varepsilon > 0$. The volumes of the outer shell Σ_ε and the blade $\mathcal{V}_\varepsilon$ are not accounted for in Eq. 2 and tend to disappear as $\varepsilon \to 0$. Likewise, the interdiscal spaces I_j for $j \in \{1,\ldots,n_*\}$ where activation occurs cannot be compounded in the remaining interdiscal spaces, since they compound the activation sources that do not vanish as $\varepsilon \to 0$, as indicated by Eq. 18. To recover the physical contributions of these regions to the diffusion process, as $\varepsilon \to 0$, the blades $\mathcal{B}_\varepsilon$, the outer shell Σ_ε, and the activated interdiscal spaces I_j, for $j \in \{1,\ldots,n_*\}$, are concentrated, in the sense that, within them, the diffusion coefficients and the mass capacities are multiplied by a factor of the order of ε^{-1} to compensate for their vanishing thickness. This way, for $\varepsilon > 0$, the system in Eq. 12 is replaced by a system of diffusion equations with discontinuous coefficients which become unbounded as $\varepsilon \to 0$. The boundary conditions Eqs. 18 and 19 for [cGMP], and Eqs. 20 and 21 for $[Ca^{2+}]$, remain unchanged. The solutions of such a three-dimensional model with discontinuous and unbounded coefficients are denoted by $[cGMP]_\varepsilon$ and $[Ca^{2+}]_\varepsilon$.

In the limit, as $\varepsilon \to 0$, the two-dimensional incisures $\mathcal{V}_\varepsilon$ tend formally to the one-dimensional segment

$$\mathcal{V} = \{r_o < x_1 < R\} \times \{x_2 = 0\}, \tag{22}$$

and the disk with incisure D_R–$\mathcal{V}_\varepsilon$ tends formally to the incised disk D_R–$\mathcal{V}$ as in Fig. 4, right. The three-dimensional outer shell Σ_ε given by Eq. 3 tends formally to the two-dimensional cylindrical surface

$$\begin{aligned}\Sigma &= \{(\bar{x}, z) | |\bar{x}| = R; z \in (0, H)\} \\ &= \{(R, \theta, z) | \theta \in [0, 2\pi); z \in (0, H)\}.\end{aligned} \tag{23}$$

Formally, the ROS tends to the cylindrical domain in Fig. 3, right, whose interior is Ω–$\mathcal{B}$ and whose lateral boundary is $\Sigma \cup \mathcal{B}$.

The rigorous calculation of the limiting problem and its pointwise interpretation is presented in Andreucci et al. (30). As a way of extracting the biophysical laws of such a limiting diffusion process, here we indicate what the limiting equations look like for cGMP only. Also, to simplify the presentation and convey the main ideas we will assume that the ROS has only one incisure as in Fig. 3 and that there is only one activated face; say, for example, $F_{j_*}^-$ at the level $z_* = z_{j*}$. The numerical simulation we present in the coming sections allow for multiple incisures and multiple activation sites.

As $\varepsilon \to 0$, the approximating functions $[cGMP]_\varepsilon$ and $[Ca^{2+}]_\varepsilon$, generate four pairs of functions:

- [cGMP] and $[Ca^{2+}]$, defined in Ω–$\mathcal{B}$ and called the ''interior limit''. They satisfy a two-dimensional diffusion process (diffusion occurs only along the transversal variables $\bar{x} = (x_1, x_2)$, on each level z and on each incised disk D_R–$\mathcal{V}$.
- $[cGMP]_s$ and $[Ca^{2+}]_s$, defined in Σ and called ''limit in the outer shell''. They satisfy two-dimensional surface diffusion processes on the limiting outer shell Σ and they glue together along Σ the diffusion processes of the indicated interior limit.
- $[cGMP]_\mathcal{B}$ and $[Ca^{2+}]_\mathcal{B}$, defined on the longitudinal, limiting rectangle $\mathcal{B}$ and called ''limit in the blade'' $\mathcal{B}$. They satisfy two-dimensional surface diffusion processes on the limiting blade $\mathcal{B}$ and they glue together along $\mathcal{B}$ the diffusion processes of the indicated interior limit. They are linked to the interior diffusion process through the interior limits [cGMP] and $[Ca^{2+}]$, and to the diffusion process on the limiting outer shell Σ, through the limiting functions $[cGMP]_s$ and $[Ca^{2+}]_s$.
- $[cGMP]_*$ and $[Ca^{2+}]_*$, defined on the disk $(D_R$–$\mathcal{V}) \times \{z_{j*}\}$, and called ''limit at the activation sites''. They satisfy diffusion processes that directly respond to activation and transmit the signal to the rest of the ROS.

These functions are smooth off the activation level $z = z_{j*}$, and satisfy the usual compatibility conditions; for example,

the interior limit [cGMP] computed on Σ equals $[\mathrm{cGMP}]_s$. The same interior limit [cGMP] computed on $\mathcal{B}$ equals $[\mathrm{cGMP}]_{\mathcal{B}}$. However, [cGMP] computed for z_* is not $[\mathrm{cGMP}]_*$. The limiting equations contain the limiting forcing terms generated by Eq. 18. To simplify the symbolism set,

$$F(\bar{x},z,t) \stackrel{\text{def}}{=} \alpha - \beta_{\text{dark}}[\mathrm{cGMP}]$$
$$F_*(\bar{x},t) \stackrel{\text{def}}{=} \alpha_* - \beta_{\text{dark}}[\mathrm{cGMP}]_*$$
$$G_*(\bar{x},t) \stackrel{\text{def}}{=} k^*_{\sigma;\text{hyd}}[\mathrm{PDE}^*]_\sigma[\mathrm{cGMP}]_*. \quad (24)$$

Here, α and α_* are defined in Eq. 16 for $[Ca^{2+}]$ and $[Ca^{2+}]_*$ representing the interior limit and the limit, respectively, on the activated level z_* of the approximating $[Ca^{2+}]_\varepsilon$.

The interior limit [cGMP]

The interior limit [cGMP] satisfies

$$\frac{\partial}{\partial t}[\mathrm{cGMP}] - \mathrm{D}_{\mathrm{cG}}\Delta_{\bar{x}}[\mathrm{cGMP}] = F \quad \text{in} \quad \Omega - \mathcal{B}. \quad (25)$$

Here, $\Delta_{\bar{x}}$ is the Laplacian acting only on the transversal variables $\bar{x} = (x_1, x_2)$. Since $[\mathrm{cGMP}](\bar{x},z,t)$ is a function of the transversal variables $\bar{x}$ and the longitudinal variable z, these can be regarded as a family of diffusion processes, parameterized with $z \in (0, H)$, each taking place on the incised disk D_R–$\mathcal{V}$. The homogenized limit transforms the boundary fluxes in Eq. 18 into volumic source terms holding in Ω–$\mathcal{B}$. Finally the initial datum $[\mathrm{cGMP}]_{\text{dark}}$ is preserved in the limit.

The limit $[\mathrm{cGMP}]_*$ on the activated level z_*

The limiting $[\mathrm{cGMP}]_*$ satisfies the diffusion process

$$\frac{\partial}{\partial t}[\mathrm{cGMP}]_* - D_{\mathrm{cG}}\Delta_{\bar{x}}[\mathrm{cGMP}]_* = F_* - G_* \quad \text{on } (D_R - \mathcal{V})\times\{z_*\}. \quad (26)$$

Therefore, the volumic diffusion in Eq. 12 is transformed into a two-dimensional diffusion on the layer $(D_R$–$\mathcal{V}) \times \{z_*\}$. The flux terms in Eq. 18 are transformed into sources defined on the incised disk D_R–$\mathcal{V}$ at the level z_*. Notice that in this case the limiting equation contains the limiting forcing term G_* due to activation. The initial datum $[\mathrm{cGMP}]_{\text{dark}}$ is preserved in the limit.

The limit $[\mathrm{cGMP}]_{\mathcal{B}}$ on the limiting incisure $\mathcal{B}$

The coordinates on $\mathcal{B}$ are $r \in (r_o, R)$ and $z \in (0, H)$. For $\varepsilon = \varepsilon_o$, the ROS is in its physical configuration and we denote by $r \to \theta_{\varepsilon_o}(r)$ the polar description of the physical incisure for $\varepsilon = \varepsilon_o$, i.e., before the homogenization starts. For example, $2R\theta_{\varepsilon_o}(R)$ is the length of the arc cut by the physical incisure $\mathcal{V}_{\varepsilon_o}$ on the rim of the disk D_R. This we take as the width of the incisure. Then in $\mathcal{B}$,

$$2r\theta_{\varepsilon_o}(r)\frac{\partial}{\partial t}[\mathrm{cGMP}]_{\mathcal{B}} - \mathrm{div}_{r,z}(2r\theta_{\varepsilon_o}(r)D_{\mathrm{cG}}\nabla_{r,z}[\mathrm{cGMP}]_{\mathcal{B}})$$
$$= (1-\gamma_o)D_{\mathrm{cG}}\{[\mathrm{cGMP}]^+_{x_2} - [\mathrm{cGMP}]^-_{x_2}\} + \delta_{z_*}\nu\varepsilon_o D_{\mathrm{cG}}\{[\mathrm{cGMP}]^+_{*,x_2} - [\mathrm{cGMP}]^-_{*,x_2}\}. \quad (27)$$

Here, $[\mathrm{cGMP}]^{\pm}_{x_2}$ is the limit of the x_2-derivative of the interior limit [cGMP], as (x_1, x_2) tends to the limiting incisure $\mathcal{B}$ from $x_2 > 0$ and $x_2 < 0$, respectively. Thus the first term on the right-hand side is the outward flux of the interior limit [cGMP] from Ω–$\mathcal{B}$ into $\mathcal{B}$. In the second term, δ_{z*} is the Dirac mass in $\mathcal{B}$ concentrated on the segment $\mathcal{B} \cap \{z = z_*\}$, whereas $[\mathrm{cGMP}]^{\pm}_{*,x_2}$ are defined as before for the limit $[\mathrm{cGMP}]_*$ on the activated incised disk $(D_R$–$\mathcal{V}) \times \{z_*\}$. In summary, the limit $[\mathrm{cGMP}]_{\mathcal{B}}$ satisfies a diffusion process on $\mathcal{B}$, whose forcing terms are the outward flux of the interior limit [cGMP] and the limit $[\mathrm{cGMP}]_*$ on the activated disk. The coefficients of such fluxes reflect the original geometry of the ROS through the parameters γ_o, ν, and ε_o. The initial datum $[\mathrm{cGMP}]_{\text{dark}}$ is preserved as well, as the no-flux condition on the top and bottom of the ROS. Finally, the interior limit [cGMP], when computed on $\mathcal{B}$, equals $[\mathrm{cGMP}]_{\mathcal{B}}$, i.e.

$$[\mathrm{cGMP}]|_{\mathcal{B}} = [\mathrm{cGMP}]_{\mathcal{B}}. \quad (28)$$

Remark 1

If the ROS has m incisures, for a given positive integer m, then the limiting homogenization process gives rise to m limiting incisures $\mathcal{B}_j$ for $j = 1,2,\ldots,m$. In such a case, Eq. 27 is replaced by m equations each holding on $\mathcal{B}_j$, where, in the right-hand side, the flux of [cGMP] and $[\mathrm{cGMP}]_*$ is meant across $\mathcal{B}_j$.

Remark 2

If there are multiple activation sites—say, for example, z_{j*} or $j_* \in \{1, 2, \ldots, n_*\}$—then the last term in Eq. 27 is replaced by n_* terms of the same form and each holding at the levels z_{j*} for the Dirac masses $\delta_{z_{j_*}}$.

The limit $[\mathrm{cGMP}]_s$ in the outer shell

Describe the limiting, incised ROS Ω–$\mathcal{B}$ in cylindrical coordinates (ρ, θ, z) and the limiting outer shell Σ in terms of (θ, z) as in Eq. 23. Without loss of generality, the limiting incisure $\mathcal{B}$ corresponds to $\theta = 0$. The fluxes of the interior limit [cGMP] and the limit $[\mathrm{cGMP}]_*$ on the activated level z_*, across Σ and directed outside the ROS, are

$$-D_{\mathrm{cG}}[\mathrm{cGMP}]_\rho|_{\rho=R} \quad - D_{\mathrm{cG}}[\mathrm{cGMP}]_{*,\rho}|_{\rho=R} \quad \text{for } \theta \neq 0.$$

Describing $\mathcal{B}$ in terms of $r \in (r_o, R)$ and $z \in (0, H)$, the outward flux of $[\mathrm{cGMP}]_{\mathcal{B}}$ on Σ is

$$-D_{\mathrm{cG}}[\mathrm{cGMP}]_{\mathcal{B},r}|_{r=R}.$$

Then the equation satisfied by $[\mathrm{cGMP}]_\mathrm{s}$ on Σ is

$$\frac{\partial}{\partial t}[\mathrm{cGMP}]_\mathrm{s} - D_\mathrm{cG}\Delta_\Sigma[\mathrm{cGMP}]_\mathrm{s} = -\frac{(1-\gamma_\mathrm{o})D_\mathrm{cG}}{\sigma\varepsilon_\mathrm{o}}[\mathrm{cGMP}]_\rho - \delta_{\mathrm{o},z_*}\frac{\nu D_\mathrm{cG}}{\sigma}[\mathrm{cGMP}]_{*,\rho} - \delta_{\theta=0}\frac{2R\theta_{\varepsilon_\mathrm{o}}(R)D_\mathrm{cG}}{\sigma\varepsilon_\mathrm{o}}[\mathrm{cGMP}]_{\mathcal{B},\mathrm{r}}. \tag{29}$$

Here, δ_{o,z_*} is the Dirac mass on Σ concentrated on the open circle segment $\Sigma \cap \{z = z_*\} \cap \{\theta \neq 0\}$. Likewise, $\delta_{\theta=0}$ is the Dirac mass on Σ concentrated on the segment $\Sigma \cap \{\theta = 0\}$. The various geometrical parameters on the right-hand side reflect the original geometry of the ROS. Thus, the limit $[\mathrm{cGMP}]_\mathrm{s}$ on the outer shell satisfies a diffusion process on Σ by the Laplace-Beltrami diffusion operator Δ_Σ on Σ, and it is driven by the exterior fluxes generated by the remaining limiting compartments. The diffusion processes in these compartments are compatible with $[\mathrm{cGMP}]_\mathrm{s}$ in the sense that

$$[\mathrm{cGMP}]|_\Sigma = [\mathrm{cGMP}]_s \text{ and } [\mathrm{cGMP}]_*|_\Sigma(t) = [\mathrm{cGMP}]_s(\theta, z_*, t) \text{ for } \theta \neq 0, \tag{30}$$

and

$$[\mathrm{cGMP}]_\mathcal{B}(R, z, t) = [\mathrm{cGMP}]_\mathrm{s}(0, z, t) \quad \text{for } \theta = 0. \tag{31}$$

Finally, the initial datum $[\mathrm{cGMP}]_\mathrm{dark}$ is preserved, as well as the no-flux condition on the top and bottom of Σ.

the same form and each holding at the levels $z_{\mathrm{j}*}$ for the Dirac masses $\delta_{z_{\mathrm{j}*}}$.

An integral version of Eqs. 25–31

These equations have been written formally, as the limiting functions involved, [cGMP], $[\mathrm{cGMP}]_*$, $[\mathrm{cGMP}]_\mathcal{B}$, and $[\mathrm{cGMP}]_\mathrm{s}$ need not be, in general, sufficiently regular to justify the operations indicated in Eqs. 25–31. They are only well defined in a suitable weak form established in Andreucci et al. (30). Here, we report a particular case of such a weak form, which permits one to relate the fully resolved model Eqs. 25–31 to simpler models that assume the cytosol well-stirred in the transversal variables. The mathematical derivation of this weak form results from the following steps:

- Integrate Eq. 25 in $d\bar{x}$ over the limiting incised disk $(D_R - \mathcal{V}) \times \{z\}$ at the generic level $z \in (0, H)$ and multiply by $(1-\gamma_\mathrm{o})$.
- Integrate Eq. 26 in $d\bar{x}$ over the limiting, incised activated disk $(D_\mathrm{R}-\mathcal{V}) \times \{z_*\}$ and multiply formally by $\nu\varepsilon_\mathrm{o}\delta_{z_*}$.
- Integrate Eq. 27 in dr over $\mathcal{B} \cap \{z\}$ for a generic level $z \in (0, H)$.
- Integrate Eq. 29 in $d\ell$ over the rim $\partial D_\mathrm{R} \times \{z\}$ at the generic level $z \in (0, H)$ and multiply by $\sigma\varepsilon_\mathrm{o}$; here $d\ell$ is the line measure on the circle ∂D_R.
- Use the Gauss-Green theorem, the periodicity of $[\mathrm{cGMP}]_\mathrm{s}$ in the variable θ, and add the resulting equalities.

This leads to the weak formulation of

$$\begin{aligned}
&\frac{\partial}{\partial t}\Big\{\iint_{(\mathrm{D_R}-\mathcal{V})\times\{z\}}[(1-\gamma_o)[\mathrm{cGMP}] + \nu\varepsilon_\mathrm{o}\delta_{z_*}[\mathrm{cGMP}]_*]d\bar{x} \\
&\quad + \int_{\mathcal{B}\cap\{z\}} 2r\theta_{\varepsilon_\mathrm{o}}(r)[\mathrm{cGMP}]_\mathcal{B}dr + \int_{\partial\mathrm{D_R}\times\{z\}}\sigma\varepsilon_\mathrm{o}[\mathrm{cGMP}]_\mathrm{s}d\ell\Big\} \\
&\quad - D_\mathrm{cG}\frac{\partial^2}{\partial z^2}\Big\{\int_{\mathcal{B}\cap\{z\}} 2r\theta_{\varepsilon_\mathrm{o}}(r)[\mathrm{cGMP}]_\mathcal{B}dr + \int_{\partial\mathrm{D_R}\times\{z\}}\sigma\varepsilon_o[\mathrm{cGMP}]_\mathrm{s}d\ell\Big\} \\
&= \iint_{(\mathrm{D_R}-\mathcal{V})\times\{z\}}[(1-\gamma_\mathrm{o})F + \delta_{z_*}\nu\varepsilon_\mathrm{o}(F_* - G_*)]d\bar{x}.
\end{aligned} \tag{32}$$

Remark 3

If the ROS has m incisures, each located at the angles $\theta = \theta_\mathrm{j}$ for $j = 1,2,\ldots,m$, then the last term in Eq. 29 bears the sum of m terms each of similar form and each relative to the limiting incisure $\mathcal{B}_\mathrm{j}$, for the Dirac mass $\delta_{\theta=\theta_\mathrm{j}}$.

Remark 4

If there are multiple activation sites, $z_{\mathrm{j}*}$ for $j_* \in \{1,2,\ldots,n_*\}$, then the penultimate term in Eq. 29 is replaced by n_* terms of

These formal arguments can be made rigorous by the procedure of Andreucci et al. (30).

Transversally well-stirred ROS

As indicated before, we will use Eq. 32 to compare the physical significance of the space-resolved model Eqs. 25–31 versus models for which the cytosol is regarded as well-stirred in the transversal variables $\bar{x}$. For this, we impose in Eq. 32 that [cGMP] is independent of the transversal

variables $\overline{x}$. This way, [cGMP] is a function only of (z, t), and by the compatibility conditions Eqs. 28, 30, and 31, one has

$$[\mathrm{cGMP}] = [\mathrm{cGMP}]_B = [\mathrm{cGMP}]_s \quad \text{as functions of } (z,t).$$

However, $[\mathrm{cGMP}]_*$ becomes a function of t only and by the same compatibility conditions,

$$[\mathrm{cGMP}](z_*, t) = [\mathrm{cGMP}]_*(t).$$

Enforcing these conditions in Eq. 32 gives

$$\left((1-\gamma_o)\pi R^2 + 2\pi R\sigma\varepsilon_o + \int_{r_o}^{R} 2r\theta_{\varepsilon_o}(r)dr\right)\frac{\partial}{\partial t}[\mathrm{cGMP}] - \left(2\pi R\sigma\varepsilon_o + \int_{r_o}^{R} 2r\theta_{\varepsilon_o}(r)dr\right)\mathrm{D}_{\mathrm{cG}}\frac{\partial^2}{\partial z^2}[\mathrm{cGMP}] = \pi R^2(1-\gamma_o)F - \pi R^2\nu\varepsilon_o\delta_{z_*}\left(\frac{\partial}{\partial t}[\mathrm{cGMP}]_* - F_* + G_*\right). \tag{33}$$

The integral in dr over (r_o, R) is the area of a horizontal cross section of the original incisure. If the ROS contains m incisures, then each of them contributes with a similar term in Eq. 33, each with its own area depending on its geometrical shape given by $r \to \theta_{\varepsilon_o}(r)$. Thus, more generally, in the case of multiple incisures the indicated integral over (r_o, R), should be replaced by the total area exposed by the union of the incisures to a transversal cross section. Set

$$\begin{aligned} A_{\mathrm{inc}} &= \{\text{total area exposed by the incisures}\} \\ A_{\mathrm{cyt}} &= 2\pi R\sigma\varepsilon_o + A_{\mathrm{inc}} \\ &\quad \{\text{horizontal cross section cytoplasmic area}\} \\ A_{\mathrm{tot}} &= (1-\gamma_o)\pi R^2 + 2\pi R\sigma\varepsilon_o + A_{\mathrm{inc}} \\ &\quad \{\text{total area of horizontal cross section}\}. \end{aligned} \tag{34}$$

Then, Eq. 33 takes the more concise form of

$$\frac{\partial}{\partial t}[\mathrm{cGMP}] - \frac{A_{\mathrm{inc}}}{A_{\mathrm{tot}}}\mathrm{D}_{\mathrm{cG}}\frac{\partial^2}{\partial z^2}[\mathrm{cGMP}] = \left(1-\frac{A_{\mathrm{inc}}}{A_{\mathrm{tot}}}\right)F - \left(1-\frac{A_{\mathrm{inc}}}{A_{\mathrm{tot}}}\right)\frac{\nu\varepsilon_o}{1-\gamma_o}\delta_{z_*}\left(\frac{\partial}{\partial t}[\mathrm{cGMP}]_* - F_* + G_*\right). \tag{35}$$

Remark 5

This equation has been derived formally from Eqs. 25–31, which are themselves formal. It can be justified rigorously as follows. First one writes Eqs. 25–31 in the weak formulation established in Andreucci et al. (30). Then one regards the ROS as an anisotropic medium with different diffusivities along the longitudinal direction z and along the transversal cross-section $\overline{x}$; say, for example, $D_{\mathrm{cG,long}}$ and $D_{\mathrm{cG,trasv}}$, respectively. By keeping $D_{\mathrm{cG,long}}$ fixed, one lets $D_{\mathrm{cG,trasv}} \to \infty$. The corresponding family of problems has a rigorous limit that satisfies Eq. 35. Physically this corresponds to assuming that cGMP diffuses with infinite speed along the transversal variables.

THE ACTIVATION MECHANISM

All terms in the homogenized system Eqs. 22–31 are well defined and their physical meaning is well identified, except for the term $[\mathrm{PDE}^*]_\sigma$ appearing in the definition of $G_*(\overline{x}, t)$ in Eq. 24, and consequently on the right-hand side of Eq. 26. The latter contains the incipient dynamics of the $[\mathrm{cGMP}]_*$, through $[\mathrm{PDE}^*]_\sigma$ which, in turn, is determined by the activation mechanism. The literature contains several attempts to model such a mechanism (15,20–22,31–33). A satisfactory modeling of the function $[\mathrm{PDE}^*](\overline{x}, t)$ for $\overline{x} = (x_1, x_2)$ ranging over the faces of the activated disk $C_{\mathrm{j}*}$, would have to take into account the full dynamics of *receptor* → *transducer* → *effector*. We propose here a model that bypasses the intermediate effect of the transducer and connects directly the activated receptor Rh* to the activated effector $[\mathrm{PDE}^*]_\sigma$. Such a point of view appears in the modeling ideas of Pugh and Lamb (15) and Nikonov et al. (22), for a well-stirred ROS, where no spatial resolution is included in the process. Thus these studies neglect the dynamics and the local effects of Rh* and $[\mathrm{PDE}^*]_\sigma$. Our model is intended to trace the surface dynamics of these molecules on their activated disk. Let $\mathrm{E}^*(t)$ denote the surface density of the number of γ subunits that have been removed from PDE. Full activation is assumed, that is, a molecule of PDE is defined to be activated if both of its γ subunits have been removed. Thus in particular if PDE* and E* are uniformly distributed on n^* activated disks,

$$[\mathrm{PDE}^*]_\sigma = \frac{\text{number of molecules of PDE}^* \text{ in the ROS}}{n^*\pi R^2} \overset{\text{def}}{=} \frac{\frac{1}{2}\mathrm{E}^*}{n^*\pi R^2}.$$

PDE* diffuses on the activated disk

$$\mathcal{D} = (D_{\mathrm{R}} - \mathcal{V}) \times \{z_*\}.$$

This is the disk D_{R}, at the level z_* of the activation site, along the axis of the ROS, from which the limiting incisure $\mathcal{V}$ has been removed. Indeed, such an incisure acts as a physical barrier to the free diffusion of PDE*, or any molecule in $\mathcal{D}$. Therefore, $\overline{x} \to E^*(\overline{x}, t)$ is a function defined on $\mathcal{D}$ that satisfies a diffusion equation there. Initially, when activation starts, $E^*(\overline{x}, 0) = 0$. As time evolves, $E^*(\overline{x}, t)$ is generated by the presence of Rh* and depleted because of recovery. Thus,

$$\frac{\partial}{\partial t}E^* - D_{\mathrm{E}^*}\nabla^2 E^* = \begin{Bmatrix}\text{source terms}\\ \text{due to Rh}^*\end{Bmatrix} - \begin{Bmatrix}\text{depletion terms}\\ \text{due to recovery}\end{Bmatrix},$$

where D_{E^*} is the diffusivity of E*.

Source and depletion terms

These terms have a spatiotemporal dependence, and as such, must include the contribution due to the activated transducer G*, the decay of Rh* due to recovery as well as other components in the recovery cascade. Although a full modeling is

still lacking, we propose a first spatially resolved approximation to these mechanisms. Depletion terms are proportional to E* by a deactivation rate constant k_E. To model the effects of Rh*, let $t \to \mathbf{x}(t)$ be the trajectory of a single Rh*, originating at $\mathbf{x}(0) = (x_o, y_o)$ at time $t = 0$. Then

$$\{\text{source terms due to Rh}^*\} = \nu_{RE} e^{-k_R t} \delta_{\mathbf{x}(t)},$$

where ν_{RE} is the rate of formation of E* per fully activated Rh* and k_R is the rate constant of inactivation of Rh*. The last term on the right-hand side is the Dirac mass at $\mathbf{x}(t)$, thereby signifying the local effect of the activation mechanism. Combining these remarks,

$$\begin{cases} \dfrac{\partial}{\partial t} E^* - D_{E^*} \nabla^2 E^* + k_E E^* = \nu_{RE} e^{-k_R t} \delta_{\mathbf{x}(t)} & \text{in } \mathcal{D} \\ D_{E^*} \dfrac{\partial}{\partial \mathbf{n}} E^* = 0 & \text{on } \partial\mathcal{D} \\ E^*(\cdot, 0) = 0 & \text{for } t = 0 \end{cases}, \quad (36)$$

where $\mathbf{n}$ is the outward unit normal to $\partial\mathcal{D}$. The second of these signifies that E* does not outflow the disk. This model builds on the ideas of Nikonov et al. (22) in the following sense. First, set

$$\bar{E}^*(t) = \int_{\mathcal{D}} E^*(x, y; t) dxdy.$$

This is the total number of E* on the activated disk $\mathcal{D}$, and thus on the whole ROS, since we are considering a single isomerization. If several disks are activated, such an integral would be extended to the union of the activated disks, so that, in any case, $\bar{E}^*(t)$ represents the total number of E* in the ROS. Integrating the first of Eq. 36 in $dxdy$, over $\mathcal{D}$, and using the Gauss-Green theorem and the zero-flux condition of the second of Eq. 36 gives

$$\frac{d}{dt}\bar{E}^* + k_E \bar{E}^* = \nu_{RE} e^{-k_R t},$$

irrespective of the trajectory $t \to \mathbf{x}(t)$. This is precisely the global, well-stirred model (Eqs. A1 and A2 of (22)) in the absence of background light.

A difficulty with Eq. 36 is in interpreting the first equation, since $t \to \mathbf{x}(t)$ is a random path. In Pugh and Lamb (34) it was proposed to regard Rh* as still at its activation site (x_o, y_o) and view the combined effect of *receptor* → *transducer* → *effector* as the diffusion of E* with a diffusion coefficient to be the sum of the diffusion coefficients of Rh*, G*, and E*. A rough estimate of such a cumulative diffusivity was provided in the range $2.7\ \mu m^2\ s^{-1} \le D_{E^*} \le 4.5\ \mu m^2\ s^{-1}$ according to temperature. Although this is only a first step in modeling the diffusion on the activated disks, we adopt it as a way of testing our mathematical model by numerical simulations.

Thus, on the right-hand side of the first line of Eq. 36 we have taken $\delta_{\mathbf{x}(t)} = \delta_{(x_o, y_o)}$, where (x_o, y_o) is the activation site. In our numerical simulations we have taken $D_{E^*} = 5\ \mu m^2\ s^{-1}$.

The simulations will be carried for variable (x_o, y_o), thereby tracing the effect of such a random location on the response on various parts of the ROS (close or far away from the activation site). This might be used as a way of detecting of the causes of variability of the response.

Our code is flexible enough to include a variety of ''source terms due to Rh*'' on the right-hand side of the first line of Eq. 36. For example, one might allow several isomerizations, each with its own (variable) activation sites, on the same or different disks, by setting

$$\{\text{source terms due to Rh}^*\} = \nu_{RE} e^{-k_R t} \sum_{j=1}^{m} \delta_{(x_j, y_j, z_j)}, \quad (37)$$

where m is the number of isomerizations and (x_j, y_j) are their activation sites on the homogenized disk at $z = z_j$. Another possible choice is

$$\{\text{source terms due to Rh}^*\} = \begin{cases} \nu_{RE} \delta_{(x_o, y_o)} & \text{for } 0 \le t < \tau_* \\ 0 & \text{for } t \ge \tau_* \end{cases},$$

where τ_* is a parameter that can be interpreted as a random shutoff time for Rh*. The corresponding simulations done for variable τ_* might detect another possible cause of variability of the response.

PARAMETERS

The homogenized model is rather general, and theoretically applies to the ROS of any higher vertebrate. Our numerical simulations have been performed for the Salamander for which the literature provides a reasonably complete set of values for the modeling parameters. The ranges of these parameters are collected in Tables 1 and 2, along with their sources, and our choice in the simulations. A detailed critique and justification for these ranges is in Caruso et al. (27), to which we refer for further discussion. Here we discuss those that are complementary to Caruso et al. (27), and those that, in the simulations, have been chosen slightly out of range, and justify such choices.

Parameters related to the geometry of incisures

The total area exposed by the incisures, by a transversal cross section of the Salamander ROS, is reported to be $\approx 0.82\ \mu m^2$, and the average width of a single incisure is estimated to be in the range ≈10–12 nm (18). Inspection of electron micrographs in the literature (11,12,14,16–18) suggests that there are from 15 to 30 incisures in the ROS of Salamander. Using these data we have simulated each incisure as an isosceles triangle of base 15 nm and height 4.64 μm.

Although the homogenized model regards an incisure as a segment, it remembers its original geometry through the function $\theta_{\varepsilon_o}(r)$ appearing in Eq. 27. For example, the choice of an isosceles triangle with vertex at the center of the disk amounts to choosing $\theta_{\varepsilon_o}(r)$ as constant. We point out, however, that our code is flexible enough to permit simulations with spikelike incisures as in Fig. 4, of variable opening, width, and depth.

TABLE 1 Nomenclature

Symbol	Units	Definition	Reference
α; α_{min}; α_{max}	$\mu M\ s^{-1}$	Rate of synthesis of cGMP by guanylyl cyclase.	(32); Boundary Fluxes of [cGMP]
β_{dark}	s^{-1}	Rate of cGMP hydrolysis by PDE.	(31); Boundary Fluxes of [cGMP]
B_{Ca}	—	Buffering power of cytoplasm for Ca^{2+}.	(40); Boundary Conditions for $[Ca^{2+}]$
$[Ca^{2+}]$;[cGMP]	μM	Concentration of Ca^{2+}; of cGMP.	(25); Locality of Photocurrent
D_{Ca}; D_{cG}; D_{E*}	$\mu m^2\ s^{-1}$	Diffusion coefficient for Ca^{2+}; cGMP; E*.	(25); The Full Three-Dimensional Model; Source and Depletion Terms
ε; $\nu\varepsilon$	μm	Disk thickness; interdiscal space.	Introduction
E*	subunits	Number of activated PDE subunits per ROS.	(41,42); The Activation Mechanism
f_{Ca}	—	Fraction of cGMP-activated current carried by Ca^{2+}.	(40); Boundary Conditions for $[Ca^{2+}]$
$\mathcal{F}$	$\mathcal{C}mol^{-1}$	Faraday's constant.	(40); Boundary Conditions for $[Ca^{2+}]$
H	μm	Height of the ROS.	Introduction
j	pA	Global current across the ROS lateral surface.	(23); Locality of Photocurrent
j_{dark}	pA	Dark current.	Locality of Photocurrent
j_{ex}^{sat}	pA	Saturation exchange current.	(29); Locality of Photocurrent
j_{cG}^{max}	pA	Maximal exchange current.	(21); Locality of Photocurrent
J_{dark}	$pA/\mu m^2$	Dark current density ($J_{dark} = j_{dark}/\Sigma_{rod}$).	Locality of Photocurrent
J_{loc}	$pA/\mu m^2$	Local current density.	Locality of Photocurrent
$1-J_{loc}/J_{dark}$	—	Relative response.	Locality of Photocurrent
k_{cat}/K_m	$\mu M^{-1}\ s^{-1}$	Hydrolytic efficacy of activated PDE dimer.	(41,42); Calibrating Parameters
k_E	s^{-1}	Rate constant for inactivation of PDE*.	(42); Source and Depletion Terms
k_R	s^{-1}	Rate constant for inactivation of Rh*.	(42); Source and Depletion Terms
$k_{\sigma;hyd}$	$[No./\mu m^3]^{-1}\ s^{-1}$	Surface hydrolysis rate of cGMP by PDE.	(18); Boundary Fluxes of [cGMP]
$k^*_{\sigma;hyd}$	$[No./\mu m^3]^{-1}\ s^{-1}$	Surface hydrolysis rate of cGMP by PDE*.	(33); Boundary Fluxes of [cGMP]
K_{cyc}	μM	Half max. constant for cyclase effect.	(32); Boundary Fluxes of [cGMP]
K_{cG}	μM	cGMP concentration for half-max. channel opening.	(21); Locality of Photocurrent
K_{ex}	μM	Ca^{2+} concentration for half-max. channel opening.	(29); Locality of Photocurrent
m_{cG}; m_{cyc}	—	Hill exponents.	(21,32); Locality of Photocurrent; Boundary Fluxes of [cGMP]
ν_{RE}	s^{-1}	Rate of E* formation per fully activated Rh*.	(42); Source and Depletion Terms
n; n_*	No.	Number of disks; of activated disks.	Introduction; Boundary Fluxes of [cGMP]
$[PDE]_\sigma$	No. μm^{-2}	Surface density of dark-activated PDE.	(43); Boundary Fluxes of [cGMP]
$[PDE^*]_\sigma$	No. μm^{-2}	Surface density of light-activated PDE*.	(33); Boundary Fluxes of [cGMP]
R	μm	Radius of disks.	Introduction
Rh*	No.	Number of activated rhodopsins in ROS.	The Activation Mechanism
Σ_{rod}	μm^2	Lateral surface area of ROS.	(23); Locality of Photocurrent
V_{cyt}	μm^3	Volume of the cytosol in the ROS.	(33); Boundary Conditions for $[Ca^{2+}]$
$\tilde{\Omega}_\varepsilon$	—	Domain occupied by the cytosol in the ROS.	Local Modeling and Surface-Volume Interactions

We have taken 23 equal incisures per disk, for a total area of $\approx 0.8\ \mu m^2$, as reported in Olson and Pugh (18). We have taken the average width larger than the one reported in Olson and Pugh (18); this has been traded with a shorter length, to avoid that the tip of the incisure would to go all the way to the center of the disk. Taking the width ≈ 12 nm would have required either a longer incisure or a larger number of them to keep the total exposed area to $\approx 0.8\ \mu m^2$. Again, our code has been designed to handle any one of these, or alternate, simulation scenarios.

Calibrating parameters

The remaining parameters are calibrated under the constraint that they remain within the published experimental ranges. Precisely, the simulated global current drop, after a single isomerization, with activation site at the center of the middle disk (400th disk), is to fit to the average of the seven experimental curves, kindly provided by F. Rieke (unpublished). Each of the experimental curves is shifted to start, at time $t = 0$, from the same dark current j_{dark} and normalized to $j_{dark} = 1$. Numerical simulations are fit to the average of these experimental curves for five variable parameters (D_{cG}, ν_{RE}, k_{cat}/K_m, k_E, k_R). The least-square fit was realized with these variables constrained in their published experimental ranges, for a simulation of 1.2 s, with a least-square fit not exceeding 0.06. The resulting parameters are reported in Table 2 as simulation parameters.

NUMERICAL METHODS

The mathematical techniques of homogenization and concentrated capacity, as well as the mathematical computation of the homogenized form of the limiting equations, have a high computational return. Indeed the homogenized formulation permits one to perform numerical simulations of the spatiotemporal diffusion of the second messengers in the ROS of vertebrates, taking into account any number of incisures, with any geometrical distribution, at local level. An added value is that this can be done with very little computational time cost. The relevant numerical simulations presented below are based on a specific program developed in the MATLAB

TABLE 2 Parameters of the model (for Salamander ROS)

Symbol	Units	Range of values	Used in simulation	Reference
α_{max}	$\mu M\ s^{-1}$	40–50	50	(15,22)
$\alpha_{min}/\alpha_{max}$	—	0.0–0.02	0.02	(15,22)
β_{dark}	s^{-1}	1	1	(15,22); Boundary Fluxes of [cGMP]
B_{Ca}	—	10–50	20	(15,22,44)
$[cGMP]_{dark}$	μM	2–4	3	(22,41)
$[Ca^{2+}]_{dark}$	μM	0.4–0.7	0.65	(22,41)
D_{Ca}	$\mu m^2\ s^{-1}$	15	15	(45)
D_{cG}	$\mu m^2\ s^{-1}$	50–196	160	(18,31); Calibrating Parameters
D_{E^*}	$\mu m^2\ s^{-1}$	2.7–4.5	5	(34); Source and Depletion Terms
ε_o; $\nu\varepsilon_o$	μm	0.01–0.014	0.014	(15,41)
f_{Ca}	—	0.1–0.2	0.17	(15,22)
$\mathcal{F}$	$\mathcal{C} mol^{-1}$	96,500	96,500	(15,22)
H	μm	20–28	22.4	(15,41)
j_{dark}	pA	(computed)	66	Locality of Photocurrent
j_{ex}^{sat}	pA	17–20	17	(15)
j_{cG}^{max}	pA	70–7000	7000	(22)
J_{dark}	$pA/\mu m^2$	(computed)	0.085	Locality of Photocurrent
k_{cat}/K_m	$\mu M^{-1}\ s^{-1}$	340–600	400	(22,42); Calibrating Parameters
k_E	s^{-1}	0.58–0.76	0.64	(44)
k_R	s^{-1}	1.69–3.48	2.8	(44)
$k_{\sigma;hyd}$	$\mu m^3\ s^{-1}$	—	7×10^{-5}	(27)
$k^*_{\sigma;hyd}$	$\mu m^3\ s^{-1}$	—	1	(21,27); Boundary Fluxes of [cGMP]
K_{cyc}	μM	0.10–0.23	0.135	(22,41)
K_{cG}	μM	13–32	20	(15,22,41)
K_{ex}	μM	1.5, 1.6	1.5	(22,41)
m_{cG}	—	2–3	2.5	(15)
m_{cyc}	—	2	2	(15,22,31)
ν_{RE}	s^{-1}	120, 150, 220	183	(15,22); Calibrating Parameters
n	—	~1000	800	(22,41)
$[PDE]_\sigma$	No. μm^{-2}	100	100	(15)
R	μm	5.5	5.5	(15,41)
$\sigma\varepsilon_o$	μm	0.015	0.015	(15,41)
Σ_{rod}	μm^2	—	776	(41)
V_{cyt}	μm^3	1000	1076	(41)

environment (The MathWorks, Natick, MA). It is based on finite element techniques. The weak form of the governing equations (Eqs. 25–31), established in Andreucci et al. (30), lends itself naturally to a finite element discretization.

The domains to be discretized consist of the cylinder Ω (the limiting ROS), the lateral surface Σ (the limiting outer shell), the longitudinal rectangular region $\mathcal{B}$ (the limiting incisure), and the zero-thickness activated disk $\mathcal{D} = (\mathcal{D}_R - \mathcal{V}) \times \{z_*\}$ (at the activated face F_j^-). The mathematical derivation of the model has been presented as containing only one incisure and one isomerization, to simplify the theoretical arguments and convey the main mathematical ideas. However, it remains valid, by minor modifications, for any number of incisures (of arbitrary distribution) and any number of photoisomerizations, however distributed on the ROS. Accordingly, the code we have developed is capable of incorporating any number of incisures and any number of activation sites, with any given distribution on the ROS. Thus, the code is aimed at being an operational tool to perform numerical experiments of phototransduction, in rods of different geometry and structure, under a wide spectrum of operating conditions.

A finite element mesh is created by using six-node prismatic elements for the interior of the rod, four-node rectangular elements for the outer shell and the blades relevant to each incisure, and three-node triangular elements for each of the activated disks.

Linear shape functions are used to interpolate the nodal values of the unknown quantities, [cGMP] and $[Ca^{2+}]$, in the interior of the triangular elements, whereas bilinear shape functions are used for the rectangular and prismatic elements. As a consequence, both [cGMP] and $[Ca^{2+}]$ are approximated by globally continuous functions. As the greatest rates of change of [cGMP] and $[Ca^{2+}]$ occur near the activated disk, a mesh-generation algorithm has been written to accomplish local logarithmic refinements of the mesh in a chosen region around each of the activated disks. This enables us to obtain an accurate solution using fewer elements, thereby considerably reducing the computational cost.

Special attention has been given to the implementation of the activation mechanism on the activated disk, as explained in The Activation Mechanism.

Time integration both for the diffusion problem on the activated disks and the diffusion problem of cGMP and Ca^{2+} in all the rod was performed with the Crank-Nicolson scheme, which guarantees stability and convergence without requiring too-small time steps (35). Alternatively, one might use the built-in MATLAB function (ODE solver) for the integration of differential equations.

The nonlinear forcing terms have been approximated, within each element, by interpolating their nodal values (nonlinearly depending on the unknown [cGMP] and $[Ca^{2+}]$) with the shape functions of the element. Their nodal values have been computed at the current timestep by weighting the values at the old and new time, as prescribed by the semi-implicit integration method. Accordingly, an iterative procedure has been used to advance the solution to the new time.

The numerical solutions of the partial differential equations give the (discretized) spatial distribution of [cGMP] and $[Ca^{2+}]$ in the cytosol as they evolve in time. Then the local current density $J_{loc}(\theta, z, t)$ at any point (θ, z) at any time t is obtained from Eqs. 4–7 using the values of $[cGMP](\theta, z, t)$ and

$[Ca^{2+}](\theta, z, t)$, on the outer membrane at that point (θ, z) and time t. The global current, $j(t)$, across the entire plasma membrane at time t, is the surface integral of $J_{loc}(\theta, z, t)$ over the lateral boundary of the ROS (see Eq. 9). Results are presented in terms of the global relative (or normalized) response $1-j(t)/j_{dark}$, and local normalized response $1-J_{loc}(\theta, z, t)/J_{dark}$.

The numerical simulations can be performed on a standard laptop, and the computational time for a 1.5 s simulation is of the order of 1 min.

SIMULATION RESULTS

We report the results of several numerical simulations of phototransduction on a single ROS, bearing incisures. The simulations are aimed at highlighting the effect of the presence of incisures in the rod on the local and global response of the photocurrent. In particular, the number of incisures and their geometries are varied, along with the photoisomerizations sites. As a reference configuration, we take a typical Salamander ROS, containing 23 incisures. (The relevant geometrical parameters of the incisures are discussed in Parameters Related to the Geometry of Incisures; the remaining physical parameters, their estimated values, and the corresponding values taken in the simulations, are discussed in Calibrating Parameters.)

As a benchmark, simulations have also been carried for the model well-stirred in the transversal variables and introduced in Transversally Well-Stirred ROS. To such a model, the incisures contribute through their total area—not through their geometry or distribution.

Finally, to underscore the role of the geometry in the response, the simulations have also been performed for a globally well-stirred model. This is obtained from Eq. 35, formally by letting $D_{cG} \to \infty$, and by interpreting [cGMP], as the concentration of cGMP in the whole ROS as a function of time only. The other quantities are interpreted similarly (see also (21)).

The global photocurrent as a function of the incisures

The set of simulations, shown in Figs. 5 and 6, report the global relative response $1-j(t)/j_{dark}$, over a time interval of 1.3 s as a function of the number of incisures and their geometry. In each run, the activation site was at the center of the disk at a level $z = H/2$. In Fig. 5 *A*, each of the incisures has the geometry described in Parameters Related to the Geometry of Incisures, that is, an isosceles triangle of base 15 nm and height 4.64 μm. Experiments were performed by progressively increasing the number of equal incisures from 0 to 23.

The continuous lines represent the response from the fully space-resolved, homogenized model Eqs. 25–31. They show a response progressively increasing with the number of incisures, while the peak time remains essentially constant at ~0.9 s. Thus incisures favor a larger amplitude response, with the highest response occurring for the maximum number of incisures. The most dramatic increases in photoresponse amplitude come with just one or three incisures. Increasing the number up to 23 incisures has a moderate effect.

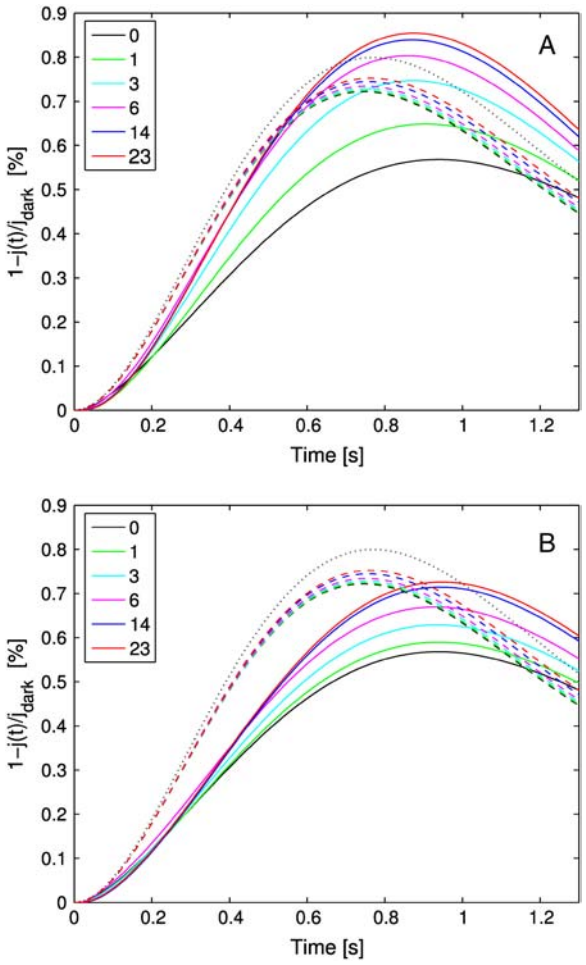

FIGURE 5 Global relative response $1-j(t)/j_{dark}$ as a function of time for an increasing number of incisures. (*Continuous lines*: tridimensional homogenized model; *dashed lines*: transversally well-stirred model; *dotted lines*: totally well-stirred model.) (*A*) Incisures with geometry as described in Parameters Related to the Geometry of Incisures (long and thin, with tip close to the activation site). (*B*) Incisures with equal area but half the length and double the width of those in panel *A* (wide and short, with tip farther away from the activation site).

The dashed lines are the responses simulated from the transversally well-stirred model Eq. 35. They also indicate an increase in the response but much less dramatic than for the fully space-resolved model. Indeed, increasing the number of incisures in this model only has an affect on the effective diffusivity, D_{cG}, through an increased value of the factor A_{inc}/A_{tot} in Eq. 35. The peak time is anticipated to be ~0.75 s, since ''transversally well-stirred'' essentially means that the transversal diffusivity is infinite.

The dotted curve is the response for the fully well-stirred model. The response is higher than the one for the transversally well-stirred model (*dashed lines*), since well-stirred essentially means that, ideally, the diffusion coefficient D_{cG}

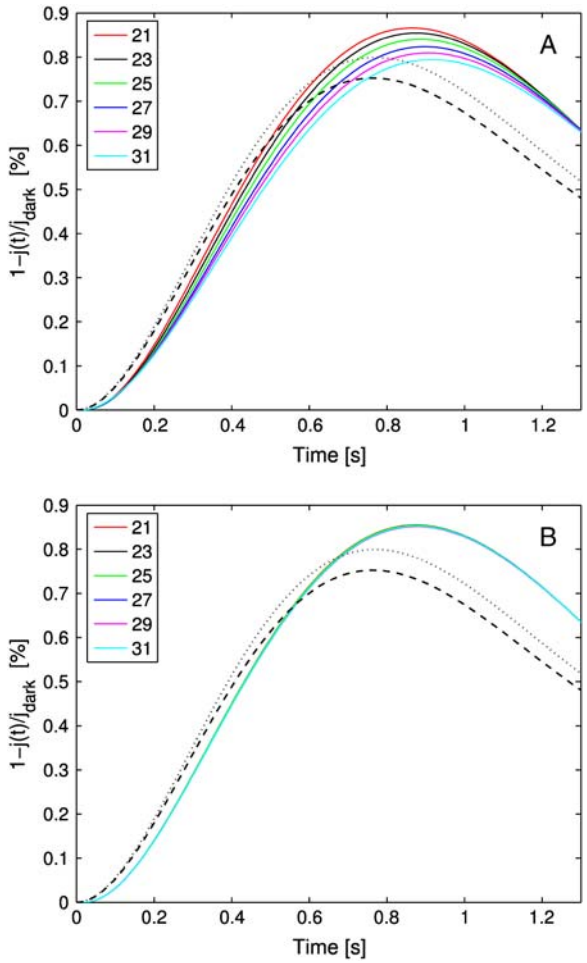

FIGURE 6 Global relative response $1-j(t)/j_{\text{dark}}$ as a function of time for an increasing number of incisures. (*Continuous lines*, tridimensional homogenized model; *dashed lines*, transversally well-stirred model; *dotted lines*, totally well-stirred model.) (*A*) The total area of the incisures and their width are kept constant. Therefore, by increasing the number of incisures, their length is reduced to keep the total area and their width constant. (*B*) The total area of the incisures and their length are kept constant. Therefore, by increasing the number of incisures, their width is reduced to keep the total area constant.

is taken to be infinity. In the simulations of Fig. 5 *B* the geometry of incisures has been changed. Namely each is an isosceles triangle of base 30 nm and height 2.32 μm so that the area of each incisure remains the same. Again, as in Fig. 5 *A*, the number of equal incisures is progressively increased from 0 to 23.

The dashed and dotted lines remain the same, since the well-stirred models, globally or transversally, are independent of the geometry of the incisures. The continuous lines exhibit a dramatic drop in response and a delay in the peak time. Thus, a redistribution of the total area of the incisures near the rim of the disk drastically opposes diffusion and results in a lower and slower response. Comparing the simulations of Fig. 5, *A* and *B*, shows that when the incisures are longer (4.64 μm in Fig. 5 *A*), and thus closer to the activation site, the relative response, for each fixed number of incisures, is larger than for shorter incisures (2.32 μm in Fig. 5 *B*), and thus further away from the activation site. In particular, for longer incisures, the response predicted by the homogenized model has a peak, for sufficiently many incisures, that is larger than the one relative to the fully well-stirred model. For shorter incisures, independently of their number, the response of the homogenized space-resolved model is always lower than that exhibited by the fully well-stirred model.

Returning briefly to the discussion of Fig. 5 *A*, it is worth noticing that, by increasing the number of incisures, the fully space-resolved model (*continuous lines*) produces a response even higher than the one for the fully well-stirred model. Such a behavior might appear paradoxical, since the latter corresponds mathematically to a model with infinite diffusivity. However, it might be explained by the role played by the geometry of the incisures versus the activation site. To stress this point, simulations have been run to compute the longitudinal flux of cGMP across horizontal sections of the ROS, generated by a single isomerization at the center of the middle disk ($z = (1/2)H$). Let $F_{\text{res}}(z, t)$ denote such a flux at level $z \in= ((1/2)H,H)$ and at time t, computed by the homogenized, space-resolved model, and let $F_{\text{tws}}(z, t)$ the same flux computed by the transversally well-stirred model. Both functions $z \rightarrow F_{\text{res}}(z, t)$ and $z \rightarrow F_{\text{tws}}(z, t)$ decrease as z increases from $(1/2)H$ to H, either in the presence or absence of incisures. For short and wide incisures, with tip away from the activation site (Fig. 5 *B*), $F_{\text{res}}(z, t) < F_{\text{tws}}(z, t)$ at all times.

For thin and long incisures, with the tip close to the isomerization site (Fig. 5 *A*), for levels z close to H, i.e., near the top of the ROS, the reversed behavior occurs; that is, $F_{\text{res}}(z, t) > F_{\text{tws}}(z, t)$.

Therefore, for the homogenized space-resolved model, long incisures with the tip close to the isomerization site have the effect of draining cGMP from regions of the ROS farther away from the isomerization site, in contrast to the analogous phenomenon for the transversally well-stirred model. Thus, channels are closed further away, thereby raising the relative response.

Analogous simulations have been run comparing the average [cGMP], as a function of time, for the globally well-stirred model and the space resolved model, for long incisures with the tip close to the activation site, as in Fig. 5 *A*. The average [cGMP] computed with the latter model is less than the corresponding one computed with the well-stirred model. These simulations provide evidence of the role of the incisures, and their geometry, as a mechanism that enhances the response even beyond that of a (virtually) well-stirred ROS.

Keeping constant the total area of the incisures

A second set of simulations is carried by increasing the number of incisures from 21 to 31, and progressively

modifying their geometry, so that the total area exposed by the incisures remains constant.

In Fig. 6 *A*, the geometry of the incisures is modified by progressively shortening their length and keeping their width constant. In Fig. 6 *B*, their length is kept constant and their width is progressively reduced to maintain constant the total exposed area. In either case, the well-stirred models (*dashed* and *dotted black curves*) return the same response, irrespective of the number of incisures or their geometry. This is expected, since these models depend on the total area of the incisures (which is kept constant), but not on their geometry or distribution.

For the space-resolved, homogenized model, distributing the area of the incisures near the activation site (Fig. 6 *A*, longer incisures of equal width or Fig. 6 *B*, equal length reduced width) enhances the diffusion process, by producing a response higher than the well-stirred models corresponding to the same total area. This dramatically underscores the role of the geometry in the process, i.e., for equal areas, the higher response is obtained by distributing the area of the incisures near the center of the activated disk. On the other hand, by distributing the area of the incisures in long and narrow segments, which therefore come closer to the activation site, the changes on concentrations are higher—producing a response essentially insensitive to the number of segments needed to keep the total area constant.

THE EFFECTS OF THE ACTIVATION SITE

Our model and the corresponding code have the capability of tracking the dependence of the response, local and global, on the activation site and simultaneously with and without incisures. In Fig. 7, a single photon hits at various distances from the center, and on the same radius. In Fig. 7 *A*, such a radius bisects two incisures. In Fig. 7 *B*, there are no incisures.

In the case of no incisures, there is a large variability in both the amplitude and time-to-peak of the response. The largest total response occurs when the activation site is at the rim of the disk and the lowest when the isomerization occurs at the center.

In the presence of incisures, the behavior is reversed; that is, the largest total response occurs for an isomerization at the center of the disk and the lowest when the photon falls at the rim. The response is larger and there is less variability in both the amplitude and time-to-peak response. A possible explanation is that when the activation site is at the center, diffusion of PDE* occurs equally on radial directions, thus reaching at the same time essentially all points of the rim. When the activation site is at the rim, diffusion of PDE* is impeded by the incisures, which confine the diffusion region; as a consequence, the cGMP drop occurs, at least for short times, essentially within the region between those two incisures.

In either case, the closer the activated site is to the rim, the faster is the response, and the smaller the peak time.

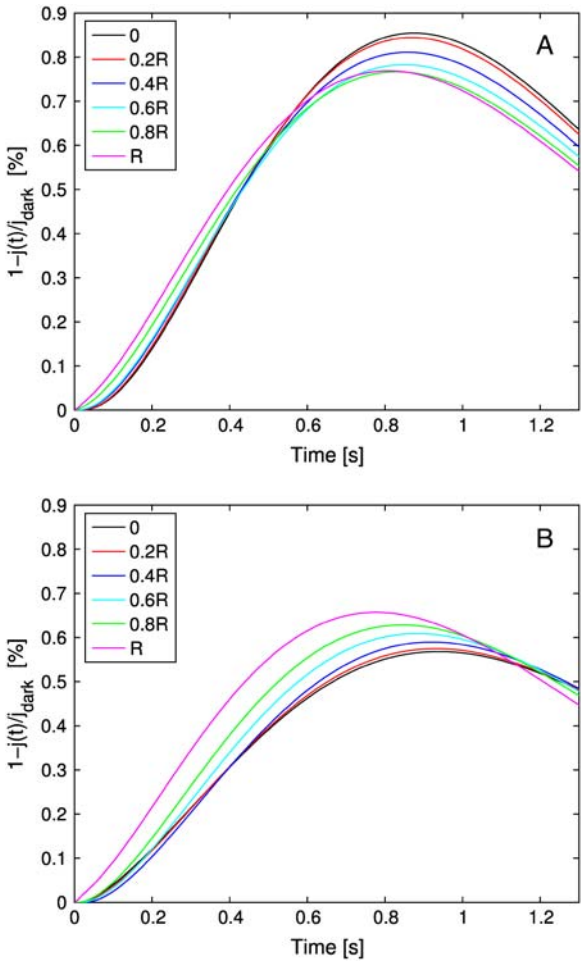

FIGURE 7 Global relative response $1-j(t)/j_{dark}$ as a function of time. (*A*) The photon hits the activated disk at different distances from the center, along a radius bisecting two consecutive incisures. The ROS has 23 incisures as described in Parameters Related to the Geometry of Incisures. (*B*) The photon hits the activated disk at different distances from the center. The ROS has no incisures.

Superposition of two single photon responses

Suppose two independent isomerizations occur, each at the center of their disk, but separated along the longitudinal axis of the ROS. It was shown in Caruso et al. (27), in the case of no incisures, that if the two activation sites are sufficiently far apart, then the response is linear in the sense that it essentially coincides with the sum of the response that each of them would generate as a SPR. It is natural to ask to what degree such an independence continues to hold in the presence of incisures, i.e., to what degree the response of such a double isomerization differs from the sum of the response that each of them would generate as a SPR. This is the content of the simulations of Figs. 8 and 9. The deviation from linear response was computed by the formula $(2p_o–p)/2p_o$. Here, p_o is the peak of SPR, with an activation site at the center of a disk sufficiently far away from the top and bottom

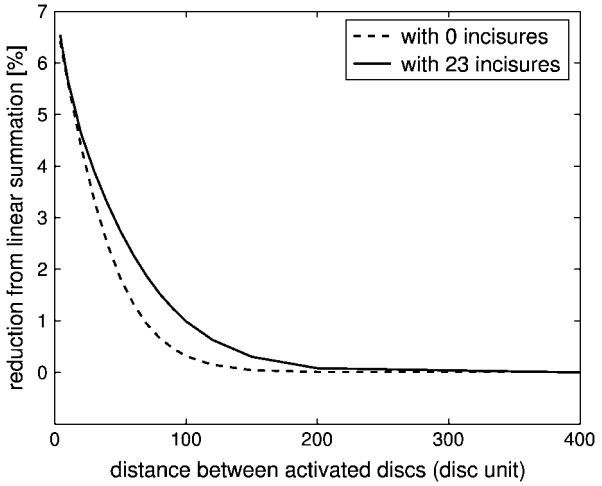

FIGURE 8 Two-photon simulations with and without incisures. The photons hit the center of two different disks. Deviation from linear sum of SPR as a percentage of maximum relative response (ordinate axis), against mutual distance of the two activated disks, measured in disk units (abscissas), is shown. Mutual distances of the two activated disks range from 400 to 4 disk units. Peak times of total relative response range from 920 ms to 940 ms for zero incisures and from 860 ms to 880 ms for 23 incisures.

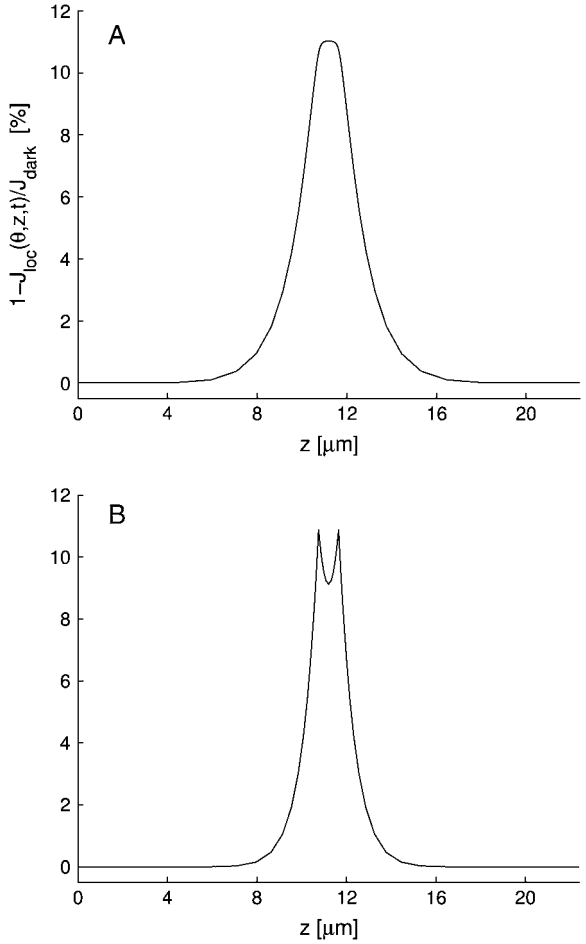

FIGURE 9 Two-photon simulations with (*A*) and without (*B*) incisures. The photons hit the center of two different disks, symmetrically placed about the middle of the ROS (400 in disk units), and separated by 16 disk units. Local relative response (ordinate axis) plotted against the z variable (abscissa).

of the ROS, and p is the peak response for the two simultaneous, symmetric isomerizations. When two photons are sufficiently far apart (at least 150 disks for zero incisures, and 200 disks for 23 incisures), (total) response is maximum at twice the SPR; thus their effect is additive. This linear summation of SPR begins to diminish when the distances get closer (at least 150 disks for zero incisure, and 200 disks for 23 incisures), as their spreads begin to overlap. The presence of incisures increases the longitudinal flux between disks, and thus increases the overlap of spreads. This phenomenon is clearly visible in the simulation of Fig. 9. As a consequence, the deviation exhibited by the simulation with incisures is always larger than the corresponding one for the simulation without incisures. Such a difference tends to become negligible when the two activated disks get closer. Globally, the total response is larger in the presence of incisures. The same issue might be addressed if two isomerizations occurred at two different locations on the same disk. Two isomerization sites are moved symmetrically along the same diameter. The deviation from linear response was computed by the formula $(2p_o–p)/2p_o$. Here p is the peak response of the symmetric pair of isomerizations, and p_o is the peak response of one element of the pair, acting alone in its position. Fig. 10 contains such simulations. In both the ROS with 23 incisures and the ROS without incisures, the deviation from linear response is never zero and increases as the mutual distance of the symmetric isomerizations decreases. If no incisures are present, the deviation is considerably larger, than the case with incisures. Thus, within a same disk, incisures dramatically increase the ability of the photoreceptor to accurately count photons. This behavior is opposite the previous case, when the activation sites were moving along the longitudinal axis of the ROS.

Since the diffusion equation of [PDE*] is linear, two simultaneous photons on the same disk produce double the amount of [PDE*]. Such an amount depletes only those molecules of cGMP on the adjacent interdiscal space. If there are no incisures, fresh cGMP inflows into the interdiscal space adjacent to the activated disk only through the outer shell. The presence of incisures, increases such an inflow.

HOW INCISURES AFFECT THE SPREAD OF THE RESPONSE

To detect how incisures affect the spread, simulations have been carried out for the activation site at several locations of the middle disk (400th disk), for the homogenized model both with and without incisures. Spread here is computed by

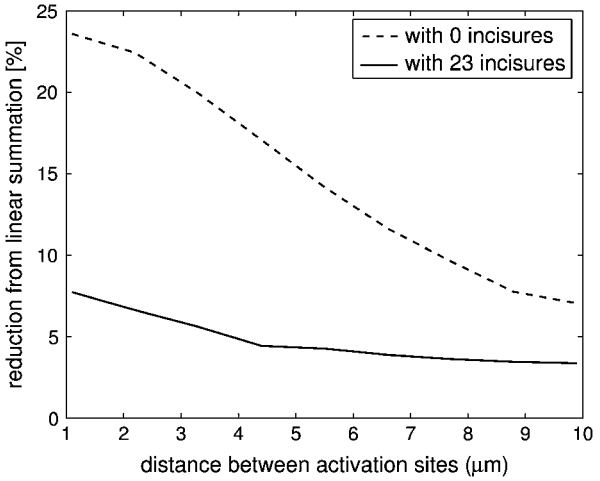

FIGURE 10 Two-photon simulations with and without incisures. The photons hit two different locations on the middle disk (400th). Deviation from linear sum of SPR as a percentage of maximum relative response (*ordinate axis*), against mutual distance of the two activation sites on the same disk, measured in microns (*abscissas*), is shown. Mutual distances of the two sites range from $0.2R$ to $1.8R$, where R is the radius of the disk. Peak times range from 790 ms to 990 ms for zero incisures and from 830 ms to 870 ms for 23 incisures.

the Eq. 11 with $\delta = 0.5\%$, as a function of θ and t. The spread was measured at different times and different recording points at the rim of the activated disk, that is, for different values of θ. The first of Figs. 11 and 12 reports the response of a ROS with 23 incisures (Fig. 11) and without incisures (Fig. 12). In both cases the activation site is at center of the middle disk and the response was computed on the rim of the disk. The last two panels of Fig. 11 and the corresponding panels of Fig. 12 report the response of a ROS with 23 incisures (Fig. 11) and without incisures (Fig. 12), where the activation site is at $0.6R$ from the center of the middle disk, and the response is computed on that point of the rim closest to ($\theta = 0$) and farthest from ($\theta = \pi$) the activation site. A spectrum of results is in Tables 3–6.

The tabulated spreads, and the figures, show that the spread is larger for 23 incisures than without incisures. This confirms the intuitive idea that the presence of incisures favors longitudinal diffusion. The enhanced longitudinal diffusion effect due the incisures is also evidenced by the rounded peaks in Fig. 11 (23 incisures present), as opposed to those in Fig. 12 (no incisures).

In addition, regardless of the point on the rim where the response is computed, the spread has, for small times, a nontrivial dependence on the activation site. As time increases to peak time, such a dependence decreases.

For a fixed off-center activation site (for example, at a distance of $0.9R$ from the center), the spread on the rim of the disk has a significant dependence on the detection position (i.e., on θ). Such an effect becomes negligible for large times (near the peak time). This phenomenon occurs both with and

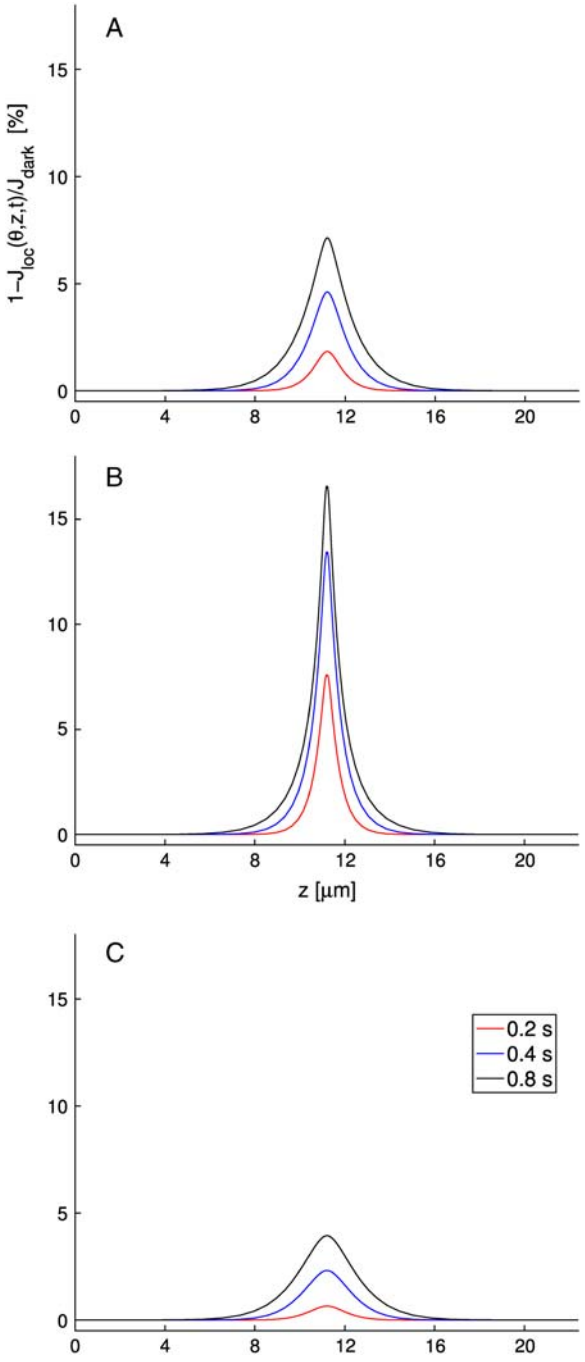

FIGURE 11 ROS with 23 incisures of total area 0.8 μm^2, as described in Parameters Related to the Geometry of Incisures. Shown are the z profiles of local relative response $1-J_{loc}(\theta, z, t)/J_{dark}$ at times 0.2 s, 0.4 s, and 0.8 s. (*A*) Activation site is at the center of the middle disk and response is measured on the rim of the disk for $\theta = 0$. (*B*) Activation site is at distance $0.6R$ from the center and the response is measured at the closest point on the rim to the activation site ($\theta = 0$). (*C*) Activation site is at distance $0.6R$ from the center and the response is measured at the farthest point on the rim from the activation site ($\theta = \pi$).

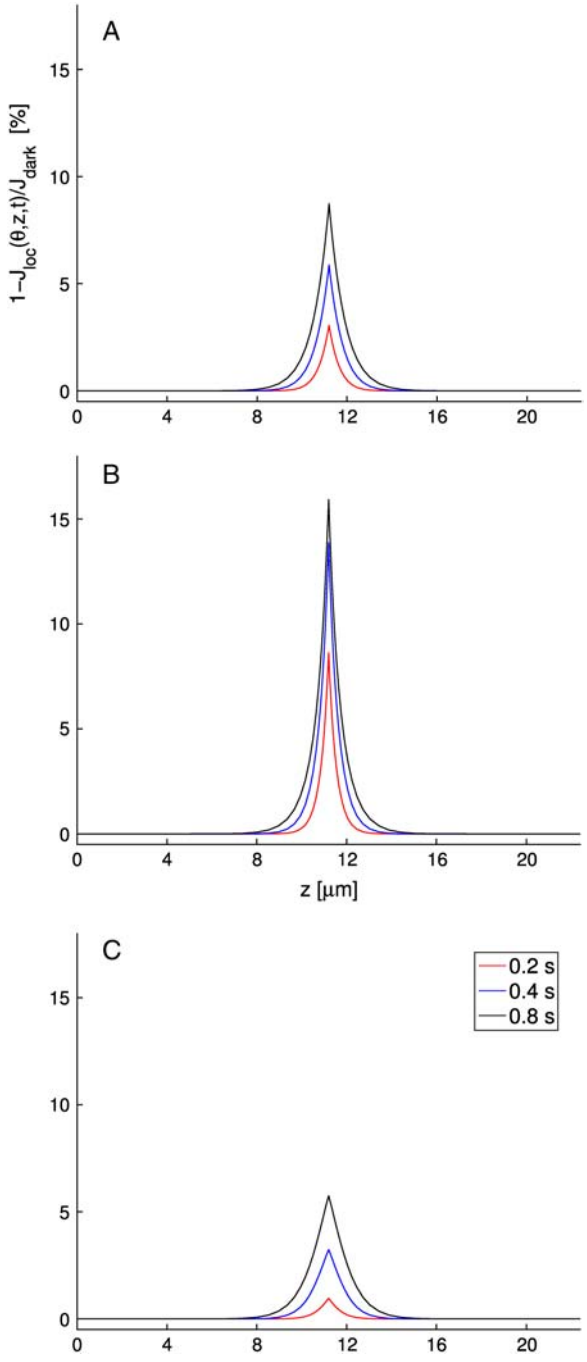

FIGURE 12 ROS with no incisures. Shown are the z profiles of local relative response $1–J_{loc}(\theta, z, t)/J_{dark}$ at times 0.2 s, 0.4 s, and 0.8 s. (*A*) Activation site is at the center of the middle disk and response is measured anywhere on the rim of the disk, since by radial symmetry, there is no θ-dependence. (*B*) Activation site is at distance $0.6R$ from the center and the response is measured at the closest point on the rim to the activation site ($\theta = 0$). (*C*) Activation site is at distance $0.6R$ from the center and the response is measured at the farthest point on the rim from the activation site ($\theta = \pi$).

without incisures, and underscores the locality of the activation process, at least up to peak time. It thus provides evidence against the notion of a transversally well-stirred model.

RADIAL PROFILES OF cGMP

Fig. 13 compares the radial profiles of [cGMP], at the z level of the activated disk, for no incisures (Fig. 13 *A*) and in presence of 23 incisures (Fig. 13 *B*). The isomerization is at the center ($\rho = 0$) of the middle disk (400th). With no incisures, immediately after activation there is a large drop of cGMP near $\rho = 0$, which persists up to the peak response. In the presence of incisures, such a drop is dramatically reduced and localized near the activation site. This phenomenon further underscores the mechanism by which further inflow of cGMP is permitted into the interdiscal spaces through the incisures.

DISCUSSION

We found that disk incisures in rod photoreceptors have two clear roles. First they provide greater cytoplasmic space for diffusion of cGMP and Ca^{2+}. This allows more communication longitudinally between disks. The greater pool of cGMP available to the PDE in the activated disk has the effect of increasing the size of the photoresponse, because more cGMP is cleaved. Moreover, it increases the linear response to multiple photons, falling on the same disk. This is illustrated clearly in Fig. 10, where two photons hit a single disk at different locations. The figure shows a dramatically increased independence between the two photons, as expressed by the decreased reduction from linear summation in the photoreceptor with 23 incisures. Also, because of the greater cytoplasmic space, there is a smaller radial fall of [cGMP] (Fig. 13). The longitudinal profile of the photoresponse is blunted (compare Figs. 11 and 12), decreasing the local nature of signaling, since cGMP diffusion is less impeded by the baffling effect of the disks. Thus the presence of many incisures has the global effect of making the local response closer to the predicted well-stirred response. This effect is most dramatic with just a few incisures (Fig. 5).

The second role of the incisures is to divide up the disk into separate domains, lobules or petals, where two-dimensional diffusion of rhodopsin, transducin, and PDE are impeded from spreading. The effect of this lobulization is a localization of the response; the closer the photon is to the rim, the greater the localization produced as the photon is

TABLE 3 Spreads of localized relative responses when the activation site is at the center ($\rho = 0$), $\delta = 0.5\%$

Angle	$\theta = 0, \frac{1}{2}\pi, \pi$	
Incisures	0	23
0.2 s	1.6108	2.1848
0.4 s	2.8171	4.2382
0.6 s	3.5566	5.5422
0.8 s	3.9876	6.2862
1.0 s	4.1068	6.4441

TABLE 4 Spreads of localized relative responses when the activation site is at $\rho = 0.6R$, $\delta = 0.5\%$

Angle	$\theta = 0$		$\theta = \frac{1}{2}\pi$		$\theta = \pi$	
Incisures	0	23	0	23	0	23
0.2 s	1.9859	2.9111	1.3805	2.1724	0.7593	1.0764
0.4 s	3.0205	4.4524	2.8394	4.2612	2.6271	3.9870
0.6 s	3.7166	5.5896	3.6423	5.4787	3.5732	5.3471
0.8 s	4.1767	6.2090	4.1257	6.1618	4.0782	6.0991
1.0 s	4.2633	6.2833	4.2241	6.2427	4.1874	6.1886

more confined by the lobule containing it. One effect of this localization is a small reduction in the response, as shown by the simulations in Fig. 8. Moreover, simulations not here reported reveal that the lobulization partially contributes in increasing the linear summation when two photons hit the same disk.

The incisures favor the longitudinal diffusion of cGMP and Ca^{2+}, and this effect depends on the number of incisures as well as their geometry and distribution. The results in Figs. 5 and 6 show that, for equal total area of incisures, a stronger response occurs for longer incisures as opposed to shorter incisures. Other simulations (not reported) show that this effect continues to hold, although to a lesser extent, for off-center activations. The geometry of the incisures, therefore, and not just their total cross-sectional area, plays a crucial role in the drop of the photocurrent. As a consequence, neither transversally well-stirred nor globally well-stirred models are able to capture these features.

The simulations show that incisures increase the amplitudes of SPR as well as their spread. Fig. 7 shows the effects of the activation sites on the global response in the presence of incisures. Without incisures, the closer the activation site is to the rim of the disk, the faster the response. With incisures, the response is larger, more uniform, but slightly slower. This greater response as well as greater stability of response will aid in the photoreceptor function as a photon counter. When two photons hit on the same disk, there is a decreased linearity of the responses (Fig. 8). The presence of incisures divides the disk into lobes, decreasing the diffusion of PDE* from one lobe to the next, and thus, dramatically increasing linearity of the responses. This again reflects the ability of incisures to increase the photon counting function of photoreceptors. Thus, incisures provide a larger, more uniform, more linear response, enabling the photoreceptor to be a more precise photon counter. This is because cGMP can diffuse better longitudinally, whereas PDE* diffusion is constrained to a local zone by the geometry of the lobelike compartments.

When two photons hit on two different disks, in the presence of incisures there is a larger response with more spread, due to the increased diffusion of cGMP through the channels made by the incisures (Fig. 9). Because of the increased spread, there is a resulting reduction from linear summation (Fig. 8). The effect on the overall signal of this mechanism is still unclear, and is the object of current investigations.

The study of longitudinal spreads and radial profiles of cGMP confirms that the presence of incisures favors longitudinal diffusion, and thus permits further influx of cGMP into the interdiscal space through incisures. The simulations in Tables 3–6 and Figs. 11 and 12 indicate the increase of longitudinal spreads. In Fig. 13, the radial profiles of cGMP show that the drop of cGMP is largely reduced by the presence of incisures. Again, these features could not be captured by well-stirred models.

These considerations suggest that one important role of incisures is to increase the ability of the photoreceptor to more precisely count photons. This is a very important design feature, suggesting one important role of incisures. Clearly, the highly specialized nature of incisures, and the fact that photoreceptors degenerate if the rds proteins that are involved in forming and stabilizing them are disrupted, we might speculate that they have other roles as well. The fact that the effects on phototransduction are attained with a relatively small number of incisures (close to maximal effect by three incisures, Fig. 5), whereas in nature, there can be a large variety of numbers of incisures, up to 30 or more, suggests that there may be other roles for incisures than these effects on phototransduction. What might such roles be? Since incisures are the sites where microtubules run all along

TABLE 5 Spreads of localized relative responses when activation site is at $\rho = 0.9R$, $\delta = 0.5\%$

Angle	$\theta = 0$		$\theta = \frac{1}{2}\pi$		$\theta = \pi$	
Incisures	0	23	0	23	0	23
0.2 s	2.4003	2.9928	1.7281	2.0236	0.9962	0.0000
0.4 s	3.3422	4.4519	3.0855	4.2091	2.8988	3.8478
0.6 s	3.9792	5.5293	3.8709	5.3900	3.7678	5.2685
0.8 s	4.3052	6.1410	4.2552	6.0803	4.2084	6.0023
1.0 s	4.3123	6.2046	4.2674	6.1517	4.2248	6.0838

TABLE 6 Spreads of localized relative responses for different activation mechanisms

Model	Well-stirred 23 incisures	Space-resolved 23 incisures
0.2 s	3.9828	3.8827
0.4 s	6.3916	6.3829
0.6 s	8.1150	8.2361
0.8 s	9.0283	9.2873
1.0 s	9.1655	10.0774

the ROS (11), incisures might play a structural or stabilizing role. The association of microtubules equidistant between incisures and plasma membranes suggests proteins linking them (11), and there are also other proteins at disk rims that play structural roles, such as peripherin/rds, responsible for autosomal dominant retinitis pigmentosa, and ABCR, the ATP-binding cassette transporter responsible for Stargardt macular dystrophy (8,9). Part of the structural role of peripherin/rds proteins is their ability to homo- and heterodimerize, and disruption of these interactions disrupts incisures (9). Other roles may be related to microtubule-associated transport proteins such as kinesin involved in transporting molecules from the inner segment (36), or microtubule binding partner proteins (37–39).

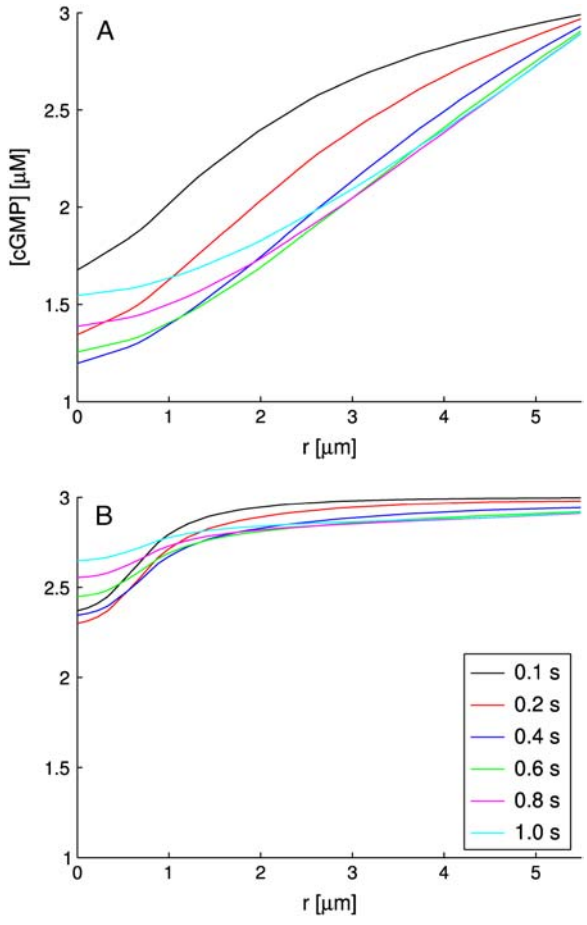

FIGURE 13 Radial profiles of [cGMP] at the activated level, with isomerization at the center of the 400th disk. Different color lines represent different times after the activation. (*A*) No incisures; (*B*) 23 incisures.

The simulations thus demonstrate that the fully space-resolved homogenized model has a great capability of capturing the physics of the problem, as it provides a theoretical, quantitative and numerical bridge from the geometry of ROS, the activation mechanism, and the diffusion of the second messengers cGMP and Ca^{2+}, to the local and global effects of the photon response. In particular, dispensing with the well-stirred limiting assumption, it permits us to detect the effects of the incisures on the drop of photocurrent (Simulation Results), to test the local effects on activation sites (The Effects of the Activation Site), and to study the longitudinal spread of the photocurrent, and the radial profiles of cGMP (How Incisures Affect the Spread of the Response and Radial Profiles of cGMP). The simulations indicate that the fully space-resolved homogenized model detects the inherent relation between the incisures and the global photocurrent.

We conclude by pointing out the flexibility of the mathematical and computational model. It presents itself as an experimental device by which biochemical and geometrical parameters, as well as activation mechanisms, can be chosen to simulate spatiotemporal responses under essentially an infinite number of physical and/virtual cross-talking situations and decision-making hypotheses.

This work was supported by National Institutes of Health grant No. 1R01GM068953-01.

REFERENCES

1. Cohen, A. I. 1960. The ultrastructure of the rods of the mouse retina. *Am. J. Anat.* 107:23–48.
2. Cohen, A. I. 1961. Some preliminary electron microscopic observations of the outer receptor segments of the retina of the *Macaca rhesus*. *In* Structure of the Eye. G. K. Smelser, editor. Academic Press, London. 151–158.
3. Cohen, A. I. 1963. The fine structure of the visual receptors of the pigeon. *Exp. Eye Res.* 2:88–97.
4. Dunn, R. F. 1966. Studies on the retina of the gecko *Coleonyx variegatus*. I. The visual cell classification. *J. Ultrastruct. Res.* 16: 651–671.
5. Nilsson, S. E. 1965. The ultrastructure of the receptor outer segments in the retina of the leopard frog (*Rana pipiens*). *J. Ultrastruct. Res.* 12: 207–231.
6. Pedler, C., and R. Tilley. 1967. The fine structure of photoreceptor disks. *Vision Res.* 7:829–836.
7. Roof, D. J., and J. E. Heuser. 1982. Surfaces of rod photoreceptor disk membranes: integral membrane components. *J. Cell Biol.* 95:487–500.
8. Poetsch, A., L. L. Molday, and R. S. Molday. 2001. The cGMP-gated channel and related glutamic acid-rich proteins interact with peripherin-2 at the rim region of rod photoreceptor disk membranes. *J. Biol. Chem.* 276:48009–48016.
9. Tam, B. M., O. L. Moritz, and D. S. Papermaster. 2004. The C-terminus of peripherin/rds participates in rod outer segment targeting and alignment of disk incisures. *Mol. Biol. Cell.* 15:2027–2037.

10. Chang, G. Q., Y. Hao, and F. Wong. 1993. Apoptosis: final common pathway of photoreceptor death in rd, rds, and rhodopsin mutant mice. *Neuron*. 11:595–605.

11. Eckmiller, M. S. 2000. Microtubules in a rod-specific cytoskeleton associated with outer segment incisures. *Vis. Neurosci.* 17:711–722.

12. Tsukamoto, Y. 1987. The number, depth and elongation of disk incisures in the retinal rod of *Rana catesbiana*. *Exp. Eye Res.* 45:105–116.

13. Papermaster, D. S., B. G. Schneider, M. A. Zorn, and J. P. Kraehenbuhl. 1978. Immunocytochemical localization of a large intrinsic membrane protein to the incisures and margins of frog rod outer segment disks. *J. Cell Biol.* 78:415–425.

14. Papermaster, D. S., P. Reilly, and B. G. Schneider. 1982. Cone lamellae and red and green rod outer segment disks contain a large intrinsic membrane protein on their margins: an ultrastructural immunocytochemical study of frog retinas. *Vision Res.* 22:1417–1428.

15. Pugh, E. N., Jr., and T. D. Lamb. 2000. Phototransduction in vertebrate rods and cones: molecular mechanisms of amplification, recovery and light adaptation. *In* Handbook of Biological Physics, Vol. 3, Molecular Mechanisms of Visual Transduction. D. G. Stavenga, W. J. de Grip, and E. N. Pugh, Jr., editors. Elsevier Science, St. Louis, MO. 183–254.

16. Liang, Y., D. Fotiadis, S. Filipek, D. A. Saperstein, K. Palczewski, and A. Engel. 2003. Organization of the G protein-coupled receptors and opsin in native membranes. *J. Biol. Chem.* 278:21655–21662.

17. Roof, D., M. Adamian, D. Jacobs, and A. Hayes. 1991. Cytoskeletal specializations at the rod photoreceptor distal tip. *J. Comp. Neurol.* 305:289–303.

18. Olson, A., and E. N. Pugh, Jr. 1993. Diffusion coefficient of cyclic GMP in salamander rod outer segments estimated with two fluorescent probes. *Biophys. J.* 65:1335–1352.

19. Holcman, D., and J. I. Korenbrot. 2004. Longitudinal diffusion in retinal rod and cone outer segment cytoplasm: the consequence of cell structure. *Biophys. J.* 86:2566–2582.

20. Gray-Keller, M., W. Denk, B. Shraim, and P. B. Detwiler. 1999. Longitudinal spread of second messenger signals in isolated rod outer segments of lizards. *J. Physiol.* 519:679–692.

21. Andreucci, D., P. Bisegna, G. Caruso, H. E. Hamm, and E. DiBenedetto. 2003. Mathematical model of the spatio-temporal dynamics of second messengers in visual transduction. *Biophys. J.* 85:1358–1376.

22. Nikonov, S., T. D. Lamb, and E. N. Pugh, Jr. 2000. The role of steady phosphodiesterase activity in the kinetics and sensitivity of the light-adapted salamander rod photoresponse. *J. Gen. Physiol.* 116:795–824.

23. Lamb, T. D., P. A. McNaughton, and K. W. Yau. 1981. Spatial spread of activation and background desensitization in toad rod outer segment. *J. Physiol.* 318:463–496.

24. Baylor, D. A., T. D. Lamb, and K. W. Yau. 1979. The membrane current of single rod outer segments. *J. Physiol.* 288:589–611.

25. Baylor, D. A., T. D. Lamb, and K. W. Yau. 1979. Responses of retinal rods to single photons. *J. Physiol.* 288:613–634.

26. Matthews, G. 1986. Spread of the light response along the rod outer segments: an estimate of the patch-clamp recordings. *Vision Res.* 26:535–541.

27. Caruso, G., H. Khanal, V. Alexiades, F. Rieke, H. E. Hamm, and E. DiBenedetto. 2005. Mathematical and computational modeling of spatiotemporal signaling in rod phototransduction. *IEE Proc. Syst. Biol.* 152:119–137.

28. Dumke, C. L., V. Y. Arshavsky, P. D. Calvert, M. D. Bownds, and E. N. Pugh, Jr. 1994. Rod outer segment structure influences the apparent kinetic parameters of cyclic GMP phosphodiesterase. *J. Gen. Physiol.* 103:1071–1098.

29. Andreucci, D., P. Bisegna, and E. DiBenedetto. 2003. Homogenization and concentrated capacity for the heat equation with nonlinear variational data in reticular almost disconnected structures and applications to visual transduction. *Ann. Mat. Pura Appl.* 182:375–407.

30. Andreucci, D., P. Bisegna, and E. DiBenedetto. 2006. Homogenization and concentrated capacity in the rod outer segment with incisures. *Appl. Anal.* 85:303–331.

31. Koutalos, Y., K. Nakatani, and K. W. Yau. 1995. Cyclic GMP diffusion coefficients in rod photoreceptors outer segments. *Biophys. J.* 68: 373–382.

32. Rieke, F., and D. A. Baylor. 1998. Origin of reproducibility in the responses of retinal rods to single photons. *Biophys. J.* 75:1836–1867.

33. Rieke, F., and D. A. Baylor. 1998. Single photon detection by rod cells of the retina. *Rev. Mod. Phys.* 70:1027–1036.

34. Pugh, E. N., Jr., and T. D. Lamb. 1993. Amplification and kinetics of the activation steps in phototransduction. *Biochim. Biophys. Acta*. 1141: 111–149.

35. Raviart, P. A., and J. M. Thomas. 1983. Introduction to Numerical Analysis of Partial Derivative Equations. Masson, Paris.

36. Eckmiller, M. S., and A. Toman. 1998. Association of kinesin with microtubules in diverse cytoskeletal systems in the outer segments of rods and cones. *Acta Anat.* (*Basel*). 162:133–141.

37. McGinnis, J. F., B. Matsumoto, J. P. Whelan, and W. Cao. 2002. Cytoskeleton participation in subcellular trafficking of signal transduction proteins in rod photoreceptor cells. *J. Neurosci. Res.* 67: 290–297.

38. Nair, K. S., S. M. Hanson, M. J. Kennedy, J. B. Hurley, V. V. Gurevich, and V. Z. Slepak. 2004. Direct binding of visual arrestin to microtubules determines the differential subcellular localization of its splice variants in rod photoreceptors. *J. Biol. Chem.* 279:41240–41248.

39. Nair, K. S., S. M. Hanson, A. Mendez, E. V. Gurevich, M. J. Kennedy, V. I. Shestopalov, S. A. Vishnivetskiy, J. Chen, J. B. Hurley, V. V. Gurevich, and V. Z. Slepak. 2005. Light-dependent redistribution of arrestin in vertebrate rods is an energy-independent process governed by protein-protein interactions. *Neuron*. 46:555–567.

40. Koutalos, Y., and K. W. Yau. 1996. Regulation of sensitivity in vertebrate rod photoreceptors by calcium. *Trends Neurosci.* 19:73–81.

41. Lamb, T. D., and E. N. Pugh, Jr. 1992. A quantitative account of the activation steps involved in phototransduction in amphibian photoreceptors. *J. Physiol.* 449:719–758.

42. Leskov, I. B., V. A. Klenchin, J. W. Handy, G. G. Whitelock, V. I. Govardovskii, M. D. Bownds, T. D. Lamb, E. N. Pugh, Jr., and V. Y. Arshavsky. 2000. The gain of rod phototransduction: reconciliation of biochemical and electrophysical measurements. *Neuron*. 27:525–537.

43. Stryer, L. 1991. Visual excitation and recovery. *J. Biol. Chem.* 226: 10711–10714.

44. Nikonov, S., N. Engheta, and E. N. Pugh, Jr. 1998. Kinetics of recovery of the dark-adapted salamander rod photoresponse. *J. Gen. Physiol.* 111:7–37.

45. Nakatani, K., C. Chen, and Y. Koutalos. 2002. Calcium diffusion coefficient in rod photoreceptor outer segments. *Biophys. J.* 82:728–739.